Improvement of soil moisture and groundwater level estimations using a scale-consistent river parameterization for the coupled ParFlow-CLM hydrological model: A case study of the Upper Rhine Basin

Samira Sadat Soltani, Marwan Fahs, Ahmad Al Bitar, Behzad Ataie-Ashtiani

Improvement of soil moisture and groundwater level estimations using a scale-consistent river parameterization for the coupled ParFlow-CLM hydrological model: A case study of the Upper Rhine Basin

Samira Sadat Soltani, [a, b] Marwan Fahs,[* b] Ahmad Al Bitar, [c] Behzad Ataie-Ashtiani [a]

[a] Department of Civil Engineering, Sharif University of Technology, Tehran, Iran

[b] Institut Terre et Environnement de Strasbourg, Université de Strasbourg, CNRS, ENGEES, UMR 7063, 67084 Strasbourg, France

[c] CESBIO, Université de Toulouse, CNES, CNRS, IRD, INRAe, UPS, 18 avenue Edouard Belin, 31401 Toulouse, France

Corresponding author

Marwan Fahs (0000-0003-0454-6476)- ORCID;

Email: fahs@unistra.fr

Samira Sadat Soltani (0000-0002-1111-1385) – ORCID;

Ahmad Al Bitar (0000-0002-1756-1096)-ORCID;

Behzad Ataie-Ashtiani (0000-0002-1339-3734)- ORCID

Abstract

Accurate implementation of river interactions with subsurface water is critical in large-scale hydrologic models with a constant horizontal grid resolution when models apply kinematic wave approximation for both hillslope and river channel flow. The size of rivers can vary greatly in the model domain, and the implemented grid resolution is too coarse to accurately account for river interactions. Consequently, the flow velocity is underestimated when the width of the rivers is much narrower than the selected grid size. This leads to inaccuracy and uncertainties in calculations of water quantities. In addition, the rate of exfiltration and infiltration between the river and the subsurface may be overestimated as the modeled area of water exchange between rivers and subsurface is larger than reality. Therefore, the present study tests the approximation of subscale channel flow by a scaled roughness coefficient in the kinematic wave equation. For this purpose, a relationship between grid cell size and river width is used to correct flow velocity, which follows a simplified modification of the Manning-Strickler equation. The rate of exfiltration and infiltration between the subsurface and river is also corrected across riverbeds by a scaled saturated hydraulic conductivity based on the grid resolution even though the grid size is relatively large. The scaling methodology is implemented in a hydrological model coupling ParFlow (PARallel FLOW) v3.5 and the Community Land Model (CLM) v4.5. The model is applied over the Upper Rhine Basin (between France and Germany) for a time period from 2012 to 2014 and at a spatial resolution of 0.055° (~6 km). The validity of the results is examined with satellite and in situ data through an innovative application of the First Order Reliability Method (FORM). The scaling approach shows that soil moisture estimates have improved, particularly in the summer and autumn seasons when cross-validated with independent soil moisture observations provided by the Climate Change Initiative (CCI). The results underline the use of a

simple scaling procedure of the Manning coefficient and saturated hydraulic conductivity to account for the real infiltration/exfiltration rate in large-scale hydrological models with constant horizontal grid resolution. The scaling procedure also shows overall improvements in groundwater level estimation, particularly where the groundwater level is shallow (less than 5 meters from the surface). By using the scaling approach, the average bias in soil moisture for the study domain was decreased from 0.17 mm^3/mm^3 to 0.1 mm^3/mm^3. The FORM results show that the probability of a substantial divergence between the ParFlow-CLM-S soil moisture results and the CCI-SM observation, which is defined as more than 0.25% of the CCI-SM observation value, is less than 0.05, 0.11, 0.15, and 0.08 for autumn, winter, spring, and summer, respectively.

Keywords: Hydrological Modeling, Scaling River Parametrization, the Upper Rhine Basin, First Order Reliability Method

1. Introduction

Hydrological modeling is an important tool for managing both environmental and water resources (Soltani, et al., 2021). Hydrological models may be applied on a large global scale (e.g., Döll et al., 2003; Kollet and Maxwell, 2006; Van Dijk et al., 2013) or on small regional scales (e.g., Christiansen et al., 2007; Huang et al., 2017). Models are still being developed to better simulate physical processes since they consider the interaction components of the water cycle, e.g., the relationship between runoff, evapotranspiration, and precipitation is included in these models (Simmons et al., 2020).

The interaction between subsurface and surface water is a numerically challenging task because surface and subsurface water do not exist as separate components of the hydrologic cycle, but rather, interact in response to topographic, soil, geologic, and climatic conditions (Eagleson,

64 1978). A common approach is to use river-routing codes, like Hydrologic Engineering Center
65 (HEC) codes, as well as MODFLOW and its River Package, to determine the head in the river
66 and then take this as the upper boundary condition of the subsurface modeling. This approach
67 does not consider the feedback between surface and subsurface models, and a better
68 representation of the physical processes in these kinds of problems is still a key challenge for
69 modelers (Kuffour et al., 2020). An integrated approach is possible, either by fully integrated
70 strong coupling where the surface and subsurface equations are solved simultaneously using a
71 nonlinear solver (Ababou et al. 2015) or by a two-way iterative coupling where the equations are
72 solved sequentially. Among the parallel integrated two-way coupled hydrologic models, ParFlow
73 simulates the surface and subsurface flow (saturated and unsaturated zone) simultaneously in 3D
74 (Maxwell et al., 2009). ParFlow has been extended to the coupled surface–subsurface flow to
75 enable the simulation of hillslope runoff and channel routing in a truly integrated fashion (Kollet
76 and Maxwell, 2006). ParFlow simulates variably saturated groundwater flow in 3D using the
77 Richard's equation (Richards, 1931). Overland flow generated by Manning's equation and the
78 kinematic wave formulations of the dynamic wave equation is considered as a boundary
79 condition in the Richard's equation (Kollet and Maxwell, 2006). This boundary condition
80 connects the subsurface flow with the land surface flow, and it removes the exchange flux term
81 from Richard's equation and calculates the movement of ponded water's free surface at the land
82 surface. The capacity of ParFlow in performing efficient 3-D simulations is relevant, as in most
83 existing models (i.e., MIKE SHE), the unsaturated flow is still calculated in 1D (Graham and
84 Butts, 2005). In addition to this capability, ParFlow is an open-access integrated model. The
85 documentation of ParFlow is relatively extensive, and it has been tested on the various surface
86 and groundwater problems in large domains (e.g., over 600 km^2) (Ferguson and Maxwell, 2012),

small basins (e.g., 30 km^2) (Kollet and Maxwell, 2006; Engdahl et al., 2016), and even subsurface–surface and atmospheric coupling (Williams et al., 2013; Shrestha et al., 2015). Since ParFlow cannot account for surface processes (e.g., evaporation) in integrated studies, ParFlow is often coupled with a land surface model and, in particular, the Common Land Model (CLM) (Kollet and Maxwell, 2008). The coupling of a surface and subsurface model improves the model complexity, bringing potentially more realism regarding the physical processes occurring at the interface between the deeper subsurface and the surface (Sulis et al., 2017; Beisman, 2007).

ParFlow is originally a grid-based hydrogeological model, and it usually calculates overland flow at much larger grid scales than the width of the rivers (Schalge et al., 2019). On the other hand, other hydrological models usually employ routing schemes for separate channels that are not related to the grid resolution (Schalge et al., 2019). When performing realistic overland flow simulations, the high computational demand of increasing the spatial resolution limits such simulations (Clark et al., 2015; Wood et al., 2011). Therefore, using the subgrid digital elevation model (DEM) was suggested for the ISBA–TRIP (Decharme et al., 2012) model, both of which are run at relatively low resolution. Neal et al. (2012) have studied the effect of subgrid scale channel routing on flood dynamics. They have shown the improvement of model performance by considering smaller channels. Therefore, applying coarse grids would increase the hydrodynamic dispersion, which indirectly reduces the peaks in the surface flows.

As an alternative to explicit subgrid channel routing, one can consider the scaling of parameters when using grid-scale river routing models (Niedda, 2004). The subscale parametrization has been suggested based on the subgrid scale topographic index by Niedda (2004). The subscale parametrization has been also used with the kinematic wave formulation for flow in rivers and

channels (Schalge et al., 2019). Thus, an approximation of the subscale channel flow by scaling Manning's roughness is used. The scaling coefficient is obtained using the relationship between the river width and the grid cell size. In order to compensate for the rate of the exfiltration and infiltration rate across the riverbeds, a grid resolution-aware scaling of saturated hydraulic conductivity is applied for the top layer (Schalge et al., 2019). By supposing a rectangular-shaped river channel cross-section, it is possible to scale both the roughness coefficient and the hydraulic conductivity. This method adds no computational cost to the model (Schalge et al., 2019). This method improves the overland-flow parametrization for the distributed hydrological models with constant horizontal grid resolution. When the subscale parametrization is not employed, the model output shows smaller river flow velocities when the streams are narrower than the horizontal grid resolution. Furthermore, the surface areas that exchange water with the subsurface in a model with wide rivers are usually larger, which causes the error of unrealistic vertical flows (Schalge et al., 2019). Scaling the roughness coefficients is appropriate when the surface water flow is governed by the open channel hydraulic performance, and therefore, it does not address the challenge of the width of the ponded area and subsequent exchanges.

To our knowledge, the scaling approach has not been tested before to improve soil moisture and groundwater level simulations, though a similar approach with substantial simplifications has been recently used to improve surface run-off in some idealized test cases (Schalge et al., 2019). In Schalge et al. (2019), without coupling by any land surface, the ParFlow model has been used to investigate the impact of scaling river parametrization. In this work, we investigate the impact of the scaling approach over the main components of the model's water budget in a real case study. We implement the scaling approach in ParFlow (Ashby and Falgout, 1996; Jones and Woodward, 2001; Kollet and Maxwell, 2006; Maxwell, 2013) version 3.5 (Kuffour, 2019),

133 which has been coupled (Maxwell and Miller, 2005; Kollet and Maxwell, 2008) with CLM (Dai
134 et al., 2003) version 4.5 (Oleson et al., 2013). The model is used to simulate the subsurface flow
135 with 0.055° (~6 km) spatial resolution over the Upper Rhine Basin between France and Germany.
136 ParFlow and CLM have been coupled to better understand the physical processes that occur at
137 the interface between the deeper subsurface and the surface. The basin studied is an important
138 hydrosystem that exists in Western Europe. Alluvial hydrosystems such as this can store large
139 quantities of water, although they are vulnerable to excessive abstraction and pollution. In the
140 present work, the domain is constructed entirely of available data sets, including topography, soil
141 texture, and hydrogeology.

142 The paper is organized as follows. Section 2 describes the geographical location of the study area
143 with an emphasis on the long-term climate condition. Section 3 provides a brief overview of the
144 equations used in the model with an emphasis on variably saturated groundwater flow, shallow
145 overland flow, and its integration in the fully coupled land surface–subsurface modeling
146 framework, and the scaling approaches for Manning's coefficient and hydraulic conductivity. In
147 addition, the land surface data and atmospheric forcing and evaluation dataset including CCI soil
148 moisture data and in situ groundwater level data are also presented. Section 4 provides details of
149 the first-order reliability method (FORM), which is a novel probabilistic validation framework
150 for validation purposes. Section 5 presents the effect of applying scaling approaches on the
151 model's results, including the temporal and spatial pattern of soil moisture and groundwater level
152 data, which is cross-validated with observations. A discussion of this paper's results with
153 previous studies is also presented in Section 5. Finally, concluding remarks are summarized in
154 Section 6.

2. Study Area: Geographical and climate condition

A major part of the Upper Rhine Basin with an area of 32.400 km^2 is located in the east of France and along the France–Germany border from Lauterbourg (north) to Basel (south), as shown in Fig. 1. The basin is separated in the west by the Vosges Mountains and in the east by the Black Forest. The Rhine alluvial aquifer is mostly made of quaternary sands and gravels. This aquifer is represented with high hydraulic conductivity from $k=10^{-4}$ to 10^{-3} m/s (Majdalani and Ackerer, 2011). The aquifer is 200 m thick at the center at the east of Colmar; however, it has a smaller thickness near the alluvial plain borders (Majdalani and Ackerer, 2011). The groundwater's main flow is toward the northern direction. In the north of the basin, the groundwater aquifer is shallow and the water surface is close to the surface. The (natural) groundwater level varies between 0 and 20 m from the surface. In other words, the mid and north parts of the aquifer have a wetlands characteristic because of the shallow groundwater depth.

Several of the river tributaries are fed by groundwater, and the river network is very dense (see Fig. 1); therefore, there is a great deal of water exchange between the surface water and groundwater resources. The River Ill is the main Rhine tributary, which originates in Sundgau, France (Thierion et al., 2012).

Precipitation is highly variable over the basin. The mountains of Vosges and the Black Forest have over 2 m per year of rainfall, whereas the annual plain average is 550 mm per year. The river changes are hugely affected by the snowfall, and it is important to consider this component, both the snowfall and melting processes. The snowfall makes up to 3% of the total precipitation in the plain, but it is much higher near the mountain peaks (37%). Therefore, the groundwater recharge is very much affected by the mountain streams. In addition, the Alpine snow melt is a significant source of large quantities of water for the Rhine River, especially at the end of spring.

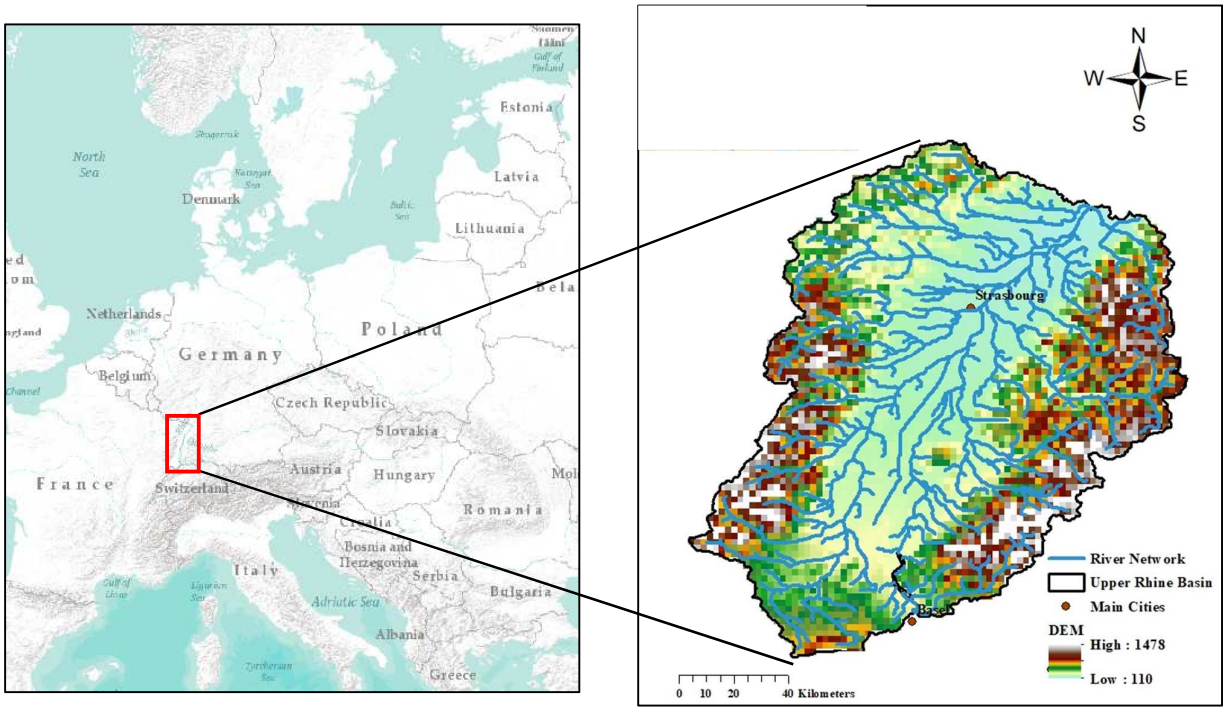

178

179 Fig. 1. Geographic location of the Upper Rhine Basin, overlaid by the Digital Elevation Model

180 (DEM) of the basin as well as the river network.

181 **3. Methods and data**

182 *3.1 Model Description*

183 In this study, the coupled surface–subsurface ParFlow (v3.5)–CLM (v4.5) hydrological model is

184 used. The CLM is a land surface model which represents the moisture, energy, and momentum

185 balances at the land surface (Dai et al., 2003). ParFlow is a groundwater model, which simulates

186 variably saturated groundwater flow in 3D using the Richard's equation (Richards, 1931).

187 ParFlow cannot account for land surface processes (e.g., evapotranspiration and snow water

188 equivalent), and the CLM generally does not simulate deeper subsurface flows. Therefore, none

189 of these models can simulate the physical processes occurring at the interface between the deeper

190 subsurface and the surface alone (Ren and Xue, 2004; Beisman, 2007; Shi et al., 2014).

191 Here we provide a brief description of ParFlow (Ashby and Falgout, 1996; Maxwell, 2013). It is
192 a groundwater flow model that considers both saturated and unsaturated flow. The surface water
193 simulator is a 2D model (Kollet and Maxwell, 2006) that uses the kinematic wave equation, and
194 the groundwater part is a 3D Richards equation solver. The Richards equation formulation
195 implemented in ParFlow is equivalent to the one in (Kollet and Maxwell, 2006)

196 $$S_S S_W(\psi_p)\frac{\partial \psi_p}{\partial t} + \phi \frac{\partial (S_W(\psi_p))}{\partial t} = \nabla.(\mathrm{q}) + q_s \quad (1)$$

197 where S_s is the specific storage coefficient [L^{-1}], S_w is the relative saturation [-], ψ_p is the
198 subsurface pressure head of water [L], t is time [T], ϕ is porosity of the medium [-], q is the
199 specific volumetric (Darcy) flux [LT^{-1}], and q_s is the general source/sink term (includes wells
200 and surface fluxes, e.g., evaporation and transpiration) [T^{-1}].
201 The water velocity is simulated using Darcy's law:

202 $$q = -K_s(\mathrm{x})K_r(\psi_p)\nabla(\psi_p - \mathrm{z}) \quad (2)$$

203 Where K_s is the saturated hydraulic conductivity, which depends on soil texture [LT^{-1}]; K_r is
204 the relative permeability [-]; q_s is the general source or sink term [T^{-1}] (includes wells and
205 surface fluxes, e.g., evaporation and transpiration); and z is depth below the surface [L].
206 The van Genuchten relationships (Van Genuchten, 1980) are utilized to define the relative
207 saturation and permeability functions as follows:

208 $$S_w(\psi_p) = \frac{s_{sat} - s_{res}}{(1+(\alpha\psi_p)^n)^{(1-1/n)}} + s_{res} \quad (3)$$

209 $$K_r(\psi_p) = \frac{\left(1 - \frac{(\alpha\psi_p)^{n-1}}{(1+(\alpha\psi_p)^n)^{(1-1/n)}}\right)^2}{(1+(\alpha\psi_p)^n)^{\frac{(1-1/n)}{2}}} \quad (4)$$

where s_{sat} [–] is the relative saturated water content, s_{res} [–] is the relative residual saturation, and α [L^{-1}] and n [–] are soil parameters. Shallow overland flow is now represented in ParFlow by the kinematic wave equation. In two spatial dimensions, the continuity equation can be written as

$$\frac{\partial \psi_s}{\partial t} = \nabla \vec{v} \psi_s + q_s \quad (5)$$

where v is the depth-averaged velocity vector [LT^{-1}], ψ_s is the surface ponding depth [L], t is time [T], and q_s is a general source/sink (e.g., rainfall) rate [LT^{-1}]. If diffusion terms are neglected, the momentum equation can be written as

$$S_{f,i} = S_{o,i} \quad (6)$$

which is commonly referred to as the kinematic wave approximation. In Eq. 6, $S_{o,i}$ is the bed slope (gravity forcing term) [–], which is equal to the friction slope $S_{f,i}$ [L]; i stands for the x and y direction. Manning's equation is used to establish a flow depth-discharge relationship:

$$v_x = \frac{\sqrt{S_{f,x}}}{n} \psi_s^{\frac{2}{3}} \quad (7)$$

$$v_y = \frac{\sqrt{S_{f,y}}}{n} \psi_s^{\frac{2}{3}} \quad (8)$$

where n is the Manning roughness coefficient [$TL^{-1/3}$]. In ParFlow, the overland flow equations are coupled directly to the Richards equation at the top boundary cell under saturated conditions. Conditions of continuity of pressure (i.e., the pressures of the subsurface and surface domains are equal right at the ground surface) and flux at the top cell of the boundary between the subsurface and surface systems are assigned. When coupled with ParFlow, the 1D soil column moisture

prediction in CLM is replaced by the ParFlow approach (in 1D or 3D formulation). In the sequential information exchange procedure, ParFlow sends the updated relative saturation (S_W) and pressure (ψ) for the top 10 layers to CLM. In turn, CLM sends the depth-differentiated source and sink terms for soil moisture [top soil moisture flux (q_{rain}), soil evapotranspiration (q_e)] for the top 10 soil layers to ParFlow (see Fig. 2a). More details on the numerical aspects and other features of the model can be found in Kollet and Maxwell (2006).

We run ParFlow for a long time (100 years) with a steady recharge force to establish the (natural) groundwater level until (natural) groundwater level and groundwater storage stop changing. Following that, we run ParFlow with CLM, performing a 5-year spin-up by simulating the time period from 2012 to 2013 five times in order to acquire equilibrium initial state variables. We have to repeat it until the differences between years are negligible (Ajamii et al., 2014; Seck et al., 2015) (here we consider differences between years to be less than 0.01 annual precipitation) to ensure that we are not gaining or losing substantial volumes of water to the subsurface over time before we start running test cases.

3.2 Land surface data and atmospheric forcing

The land surface input data include topography, land cover, soil characteristics, and physiological parameters of the canopy, which are static variables. Global Multiresolution Terrain Elevation Data 2010 (Danielson et al., 2011) was used for the Digital Elevation Model (DEM), which has a resolution of 1 km (see Fig. 1). The Moderate Resolution Imaging Spectroradiometer (MODIS) satellite land-use classification (Friedl et al., 2002) was also used, wherein it was converted to Plant Functional Types (PFT). In order to include the soil characteristics, the percentage of soil and clay were obtained using the FAO/UNESCO Digital Soil Map of the World (Batjes, 1997). This map consist of 19 classes and it is on Schaap and Leij

(1998)'s pedotransfer functions. For hydraulic characteristics of soil, such as saturated hydraulic conductivity and Van-Genuchten parameters, the Soil Grids 250 m, as well as the dataset aggregated to a 1-km resolution (Hengl et al., 2017), were used by utilizing the European pedotransfer functions (EU-PTFs; Tóth et al., 2015). For the Manning's coefficient, the proposed relationship between landcover type and Manning's coefficient is used (Asante et al., 2008).

The atmospheric forcing of the coupled ParFlow model with CLM is provided from the COSMO-REA6 data, which have a spatial resolution of 0.055° (~6 km) and daily temporal resolution, and covers the domain defined by CORDEX EUR-11(Gutowski et al., 2016). The COSMO-REA6 dataset (Bollmeyer et al., 2015), which is a reanalysis with high resolution from the Hans-Ertel Center for Weather Research, is used for the time period 2012-2014 (HErZ; Simmer et al., 2016).

German Weather Service data were used to obtain the barometric pressure, wind speed, precipitation, specific humidity, downward shortwave and longwave radiations, and air temperature near the surface. These meteorological data are available to download from the German Weather Service (DWD; ftp://ftp-cdc.dwd.de/pub/REA/). There are some uncertainties in the COSMO-REA6 data, especially the precipitation data which are used in this study Bollmeyer et al. (2015). They showed that the precipitation data from COSMO-REA6 have a relatively good performance when compared with the Global Precipitation Climatology Centre data; however, they underestimates the precipitation in middle and southern Europe and overestimate it in Scandinavia, Russia, and the beaches of Norway.

Additionally, Springer et al. (2017) assessed the closure of the water budget in the 6-km COSMO-REA6 and compared it with the global reanalysis (Interim ECMWF Reanalysis (ERA-Interim), Modern-Era Retrospective Analysis for Research and Applications, Version 2

277 (MERRA-2)) for major European river basins. In their study, Springer et al. (2017) found that
278 the COSMO-REA6 closes the water budget within the error estimates, whereas the global
279 reanalysis underestimates the precipitation minus the evapotranspiration deficit in most river
280 basins. A more comprehensive assessment of the precipitation of the HErZ reanalysis can be
281 found in Wahl et al. (2017). This analysis is based on the 2-km data product and only available
282 for central Europe. The input datasets discussed in this section are summarized in Table 1. All
283 model inputs were reprojected to have an equal cell size of 0.055° (~6 km). In this study, the
284 model was directed at the Upper Rhine Basin for a total thickness of 100 m over 300 model
285 layers with different thickness. The thickness of the soil layers increases with increasing depth.
286 The model was implemented with a horizontal resolution of 6 km with nx=31, ny=32 for a total
287 model dimension of 186 km *192 km * 100 m. This corresponds to a total number of 35712
288 cells. The hydraulic characteristics, such as saturated hydraulic conductivity and Van-Genuchten
289 parameters provided by the Soil Grids, are available only for the first two meters of soil, these
290 hydraulic characteristics for the layers are located lower than 2m are the same as the layer is
291 located at 2m under surface. Fig. 2b shows a visualization of the model. The porosity and
292 specific storage are constant and equal to 0.35 and 10^{-5}, respectively. ParFlow allows the user to
293 specify the permeability tensor. In this study, permeability is considered heterogeneous and
294 symmetric in all directions (x, y, and z), and it is specified for the whole domain and considered
295 isotropic.

296 In the ParFlow model, there is no ability to define variable depths in the domain. The only way
297 for overcoming this limitation is to define a constant depth and to assign a small value of
298 hydraulic conductivity for the layers located below the bedrock. However, this approach induces
299 numerical instabilities, leading to convergence issues. Thus, in our model, for the soil layers

300 below the bedrock, we used the same properties as for the upper layers. In other words, the
301 bedrock is located at a depth of 100 m. The hydraulic characteristics of the soil, such as saturated
302 hydraulic conductivity and Van-Genuchten parameters, are provided by the Soil Grids. These
303 parameters are available only for the first two meters of soil. Thus, the same characteristics are
304 assumed for the layers located lower than 2 m. This assumption may affect the model output, and
305 more accurate predictions could be obtained with a real database of soil characteristics for deeper
306 soil layers. Uncertainties related to the soil characteristics would certainly affect the model
307 predictions. This issue can be managed by calibrating models against observations or by data
308 assimilation. Also, uncertainty propagation or quantification analysis can be performed to
309 investigate the effect of uncertainties on the model outputs. However, this is not the objective of
310 the current study that aims at evaluating, with available data, the performance of the suggested
311 scaling approach. Two distinct boundary conditions are applied: i) In the south at Basel, the
312 Rhine River discharge is subjected to temporal variation. Rhine River discharge is implemented
313 based on streamlines of simulated fluid flow by Koltzer et al. (2019). ii) In the northern and
314 southern boundaries, a constant piezometric head is applied. A constant head boundary condition
315 is imposed based on hydraulic head measurements, which is discussed in section 3.5.1. These in
316 situ measurements are collected from observation wells in the form of sparse points and are then
317 interpolated.
318
319
320
321

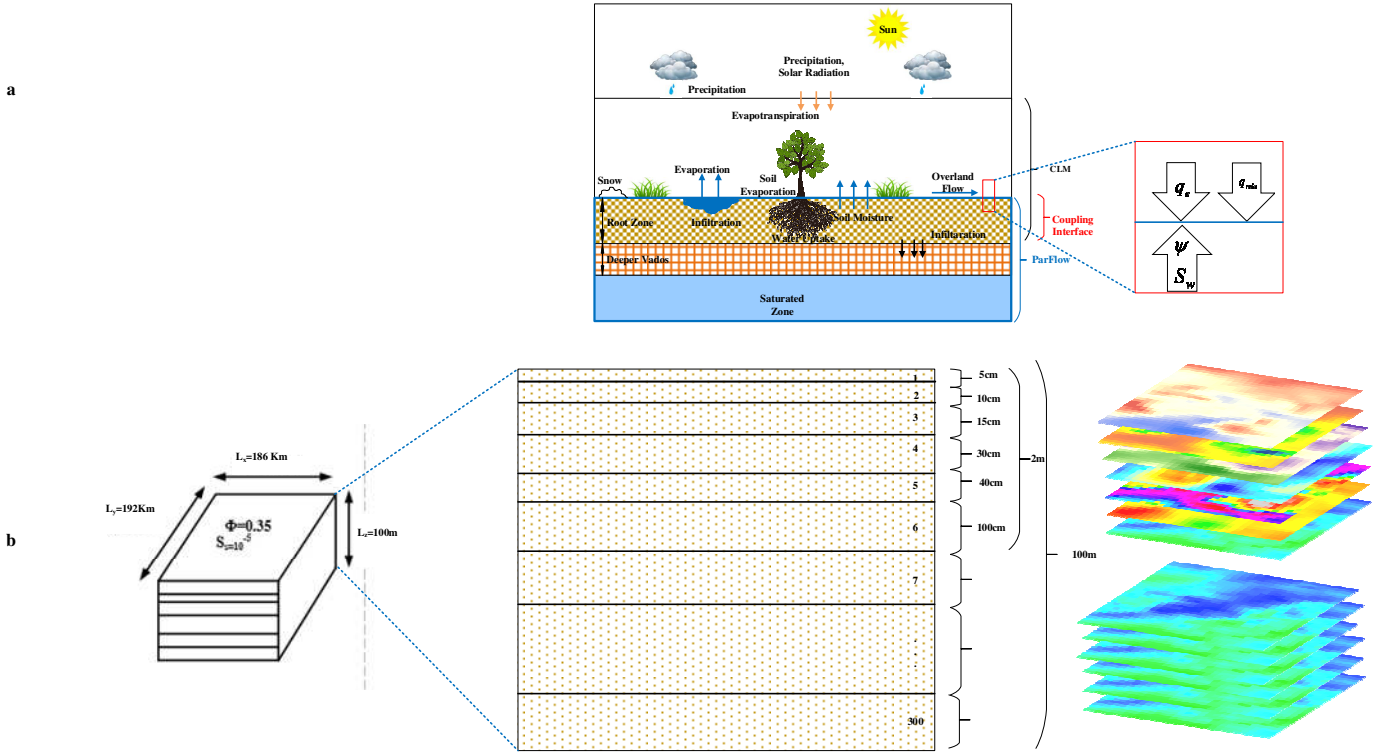

Fig. 2 a) Schematic of the coupled ParFlow-CLM model from Kuffour et al. (2020). In the bottom rectangle, ParFlow depicts the root zone, deeper vadose zone, and saturated zone. The top rectangle depicts CLM's atmospheric forcing and land surface processes. It's worth noting the root zone, where the two models exchange information about fluxes and state variables at the conceptual boundaries of the respective compartment models. The downward and upward arrows represent the pathways of information transmission between models. b) Visualization of the model including dimensions of the domain and parametrization of the aquifer. Porosity and specific storage coefficient are constant and the hydraulic characteristics such as saturated hydraulic conductivity and Van-Genuchten parameters are isotopic and non- homogenous and as the same as layer 6 for the layers 7-300.

Table 1. The input data for ParFlow-CLM

Input Data	Data Source	Download Link or Reference
Atmospheric forcing (specific humidity, near-surface air temperature, barometric pressure, wind speed, precipitation, longwave and shortwave radiation)	COSMO-REA6 dataset	ftp://ftp-cdc.dwd.de/pub/REA/
Plant Functional Type	MODIS satellite (land-use classification)	https://lpdaac.usgs.gov/products/mcd12q1v006/
Soil Texture Data, Sand and Clay Percentage	FAO/UNESCO Digital Soil Map of the World	(Batjes, 1997)
Hydraulic conductivity	European Soil Data Centre (ESDAC)	https://esdac.jrc.ec.europa.eu/content/3d-soil-hydraulic-database-europe-1-km-and-250-m-resolution
Van-Genuchten Parameters (n, α)	European Soil Data Centre (ESDAC)	https://esdac.jrc.ec.europa.eu/content/3d-soil-hydraulic-database-europe-1-km-and-250-m-resolution
DEM	Global Multiresolution Terrain Elevation Data 2010	https://earthexplorer.usgs.gov/
Manning's coefficient	Relationship between landcover type and Manning's coefficient	(Asante et al., 2008)

3.3. River Parametrization

Since ParFlow does not address the flow condition (e.g., river network) for the river, ParFlow does not distinguish between hillslope runoff and river flow, and the same horizontal grid resolution applies to the subsurface and surface water domains. Forcing the same coarse horizontal grid resolution for the subsurface and surface water domains results in an underestimation of the flow velocities, while the rate of exfiltration and infiltration between the river and the subsurface is overestimated.

Subgrid scaled river channel geometries, such as exchange fluxes with the subsurface, through the use of scaled grid scale parameters, are incorporated in modeling to compensate for this large rate of exfiltration and infiltration between the river and the subsurface. As a result, to use the overland flow boundary condition in ParFlow, we use a derived scaled Manning's coefficient (n) and saturated hydraulic conductivity (K_{sat}) by Schalge et al. (2019).

3.3.1 Manning's Coefficient Scaling

In order to correct the flow velocity (v) in the grid cell of model, which is usually greater than the river width (W_1), a scaling of Manning's coefficient is used. In an ideal high-resolution simulation, the width of the river channel (W_1) and Manning's coefficient (n_{org}), as well as the flow velocity (v_1), is considered to be the same as the real river channel. In a low-resolution model, the width of the river is considered W_2, which is equal to the width of the grid cell and greater than W_1. In this less resolution model, if we consider the same n_{org}, the flow velocity (v_2) is lower than the flow velocity in the river (v_1) because the water depth is smaller in the wider channel. Therefore, the flow velocity can be corrected by reducing n_{org} to n_{scale}. As a result, in a lower resolution simulation (grid cell is W_2), flow velocity equals v_1 (for more details refer to Schalge et al. (2019)). A simple equation is used to scale the roughness coefficient as follows:

$$n_{scale} = n_{org}.(\frac{W_1}{W_2})^{2/3} = \lambda.n_{org} \quad (9)$$

where $\lambda = (\frac{W_1}{W_2})^{2/3}$ is the scaling coefficient for Manning's roughness coefficient, which corrects the river flow velocity in a lower resolution simulation, which is independent of the channel slope (S_f) and discharge (Q) .

3.3.2 Hydraulic Conductivity Scaling

Because the width of the model river is often larger than the actual river width, a larger surface area will exchange water with the subsurface than the real river. Scaled (lower) hydraulic conductivity can be used to correct. The evaluation of the infiltration/exfiltration fluxes in the river is improved, by using scaled K_{sat}, resulting in

$$\int_{A_2} K_{sat\_scaled} dA_2 = \int_{A_1} K_{sat\_org} dA_1 \quad (10)$$

where $A_2 = W_2 \times W_2$ is the area of the river in the model and $A_1 = W_2 \times W_1$ is the area of the real river. Substitution of the A_2 and A_1 in the equation above results in

$$\int_0^{W_2}\int_0^{W_2} K_{sat\_scaled}(x,y)dxdy = \int_0^{W_2}\int_0^{W_1} K_{sat\_org}(x,y)dxdy \quad (11)$$

Where K_{sat} is homogeneous in each grid cell and, by assuming a rectangular river channel cross-section, the scaling coefficient is

$$K_{satscale} = K_{satorg} \cdot \frac{W_1}{W_2} \quad (12)$$

where $\chi = \frac{W_1}{W_2}$ is the scaling coefficient for the hydraulic conductivity (for more details refer to Schalge et al. (2019)).

3.3.3 Finding River Width

By using the Hydro SHEDS river topology dataset (database available at http://gaia.geosci.unc.edu/rivers/), as well as geomorphic relationships between parameters such as the area, discharge, width, and depth of the river, a simple database containing the widths and depths of the rivers has been created, which can be used when there are no reliable measurements available to input the initial estimation for the hydrological models. The database does not intend to replace detailed estimations of the river width and depth; instead, it maps the river characteristics with near-global coverage. However, this database provides estimations with

383 a 95% confidence interval, which gives a reasonable estimate of the width and depth of the
384 rivers.

385 The spatial width of the river for the Upper Rhine Basin is shown in Fig. 3a, and it ranges from
386 6.5 m to 325 m. In this simulation, narrow rivers with less than 10-m widths have not been
387 considered, as they only appear during and after rain.

388 Fig. 3b and 3c show the resulting scaling parameter for saturated hydraulic conductivity and
389 Manning's coefficient following Eq. (9) and Eq. (12) ranges from 0.01 to 0.16 and 0.001 to
390 0.065, respectively. Fig. 3d shows the scaling approach to which cells in the basin have been
391 applied. In this figure, the effective cells whose rivers are more than 10 m wide are blue in color,
392 and these cells have been applied to the scaled Manning coefficient and saturated hydraulic
393 conductivity. The red color in this figure indicates cells in which the width of the river is less
394 than 10 meters.

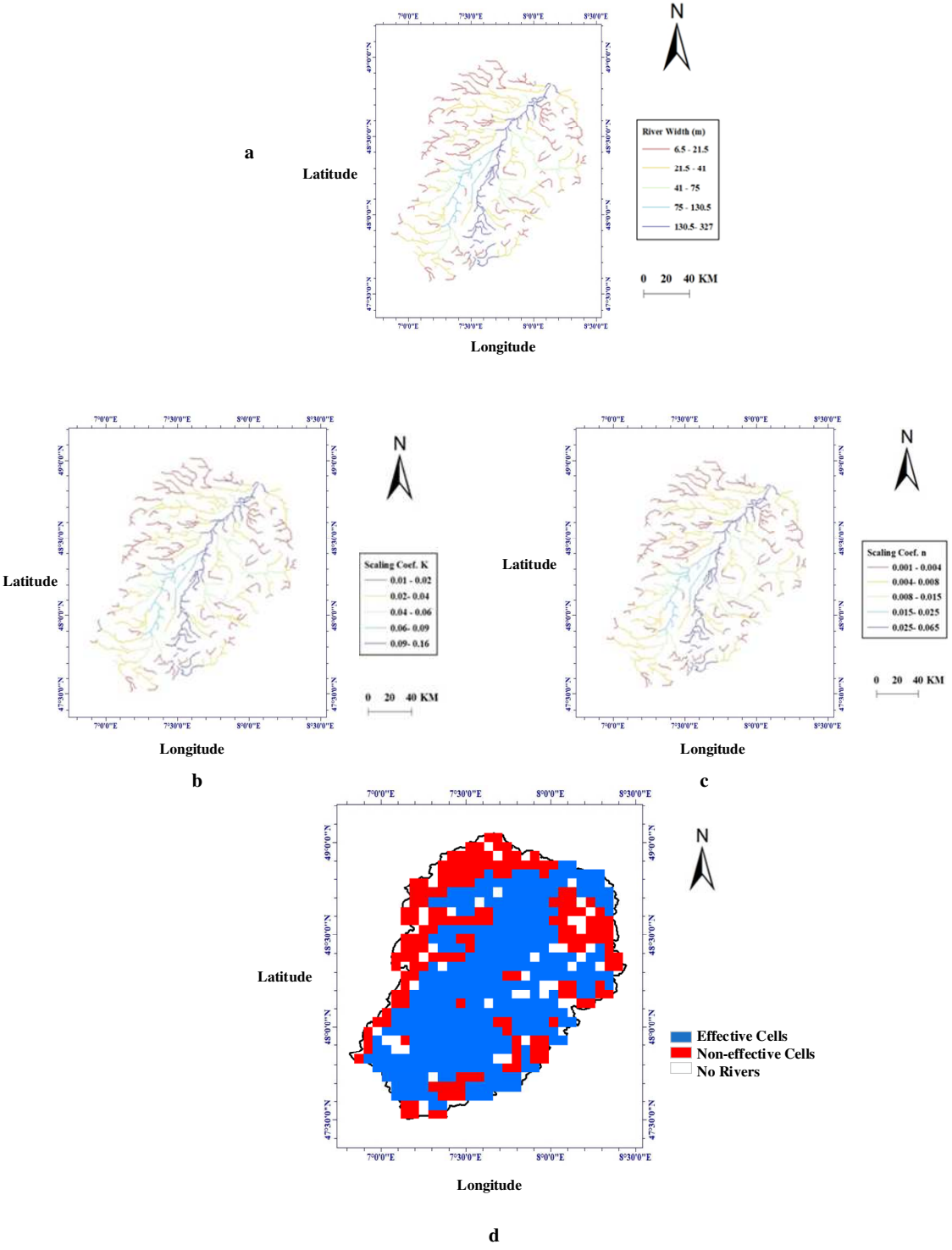

395

396 Fig. 3 a) River width (W1) in unit of meter, b) scaling coefficient of saturated hydraulic
397 conductivity, c) scaling coefficient of Manning's coefficient and d) effective and non-effective
398 cells in scaling approach over the Upper Rhine Basin

3.4. Probabilistic Framework of the Validation: First Order Reliability Method (FORM)

In this approach, a Limit State Function (LSF) is defined as the mathematical formulation of a system state limit beyond which the system reliability criteria are no longer satisfied in this method (Abdelkhalak and Bouchaïb, 2013). Analogous to the simulation results of a hydrological model, the standard deviation (SD) can be used as a criterion to examine the reliability of the model by defining LSF less than 10% as the state limit for the simulated groundwater level and 25% for the simulated soil moisture. The FORM method provides a probabilistic framework in which the LSF can be changed according to the problem. It can be defined as a combination of errors and other influencing factors. This criterion is expressed as

$$\begin{cases} SD(SM) = \dfrac{\text{Model}\,Estimation(SM) - Observation(SM)}{Observation(SM)} \le 0.1 \\ SD(Gr) = \dfrac{\text{Model}\,Estimation(Gr) - Observation(Gr)}{Observation(Gr)} \le 0.25 \end{cases} \quad (13)$$

Based on the assumption that LSF is continuous and first-order differentiable, FORM uses a linear approximation (i.e., first-order Taylor expansion) expressed as

$$G(y) = L(y) = G(y_m) + \nabla G(y_m)^T.(y - y_m) \quad (14)$$

where L(y) is the linearization of the LSF, $y = y(y_1, y_2, y_3, ...y_n)$ is the vector of n variables defining the G function, y_m is the expansion point, and ∇G(y) is the first-order gradient vector of G(y).

The two critical FORM requirements are explained in detail in the following paragraphs. (For more details refer to Soltani et al. (2020)).

1. First, project the variables X (in this case, soil moisture or groundwater level) to the independent standard normal space Y. In order to implement FORM, non-normally distributed variables should be transformed into standard normal variables (Madsen et al., 2006) via, e.g., the NATAF transformation (Nataf, 1962).

2. Next, find a point on the transformed LSF with the shortest distance to the origin in the uncorrelated standard normal space (Shinozuka, 1983). This point is called the design point (or the most probable point), and it can be obtained by solving the following constrained optimization problem:

$$y^* = \arg\min\{\|y\|\} \tag{15}$$

where y^* is the design point, which has the shortest distance to the origin in the uncorrelated standard normal space. Various approaches have been developed during the past decades to solve the constrained optimization problem described in Eq. (10). The iHLRF (Zhang and Kiureghian, 1997) is a state-of-the-art method, which can be used to obtain the point on the failure surface that is closest to the origin. In this approach, the design point is found by a generic search algorithm via the following iterative equation:

$$y_{m+1} = y_m + s_m \cdot d_m \tag{16}$$

where m is the iteration number, s is the step length, and d is the direction of the search. Let y* be the answer to this optimization problem, and β be the optimal point's distance from the origin. As a result, the estimated probability of failure is expressed as

$$P_f = \Phi(-\beta) \tag{17}$$

where Φ is the cumulative probability distribution function of β. The limitation of FORM is that it can only give an exact solution if the initial limit state is linear and the basic variables are

normally distributed. The extent of error, on the other hand, is determined by the curvature of the limit state and the method of projecting X to Y. Fig. 4 shows the general procedure of the FORM implementation.

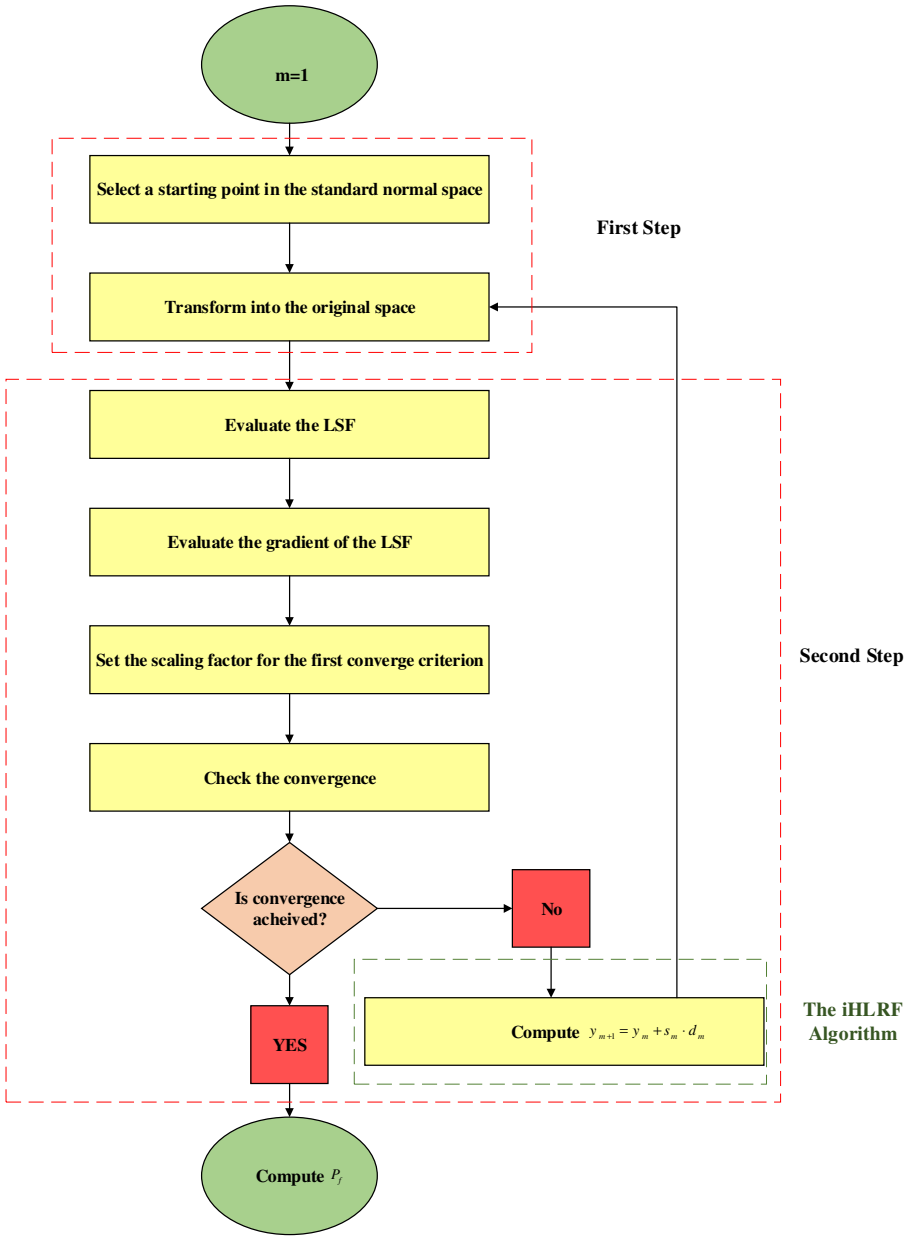

Fig. 4 Steps to implement the FORM algorithm. After defining LSF, the variables are transformed to the independent standard normal space in the first step and in the second step, a point on the transformed LSF with the shortest distance to the origin is found. The iHLRF (Zhang and Kiureghian, 1997) is used to obtain this point on the LSF.

3.5 Evaluation Dataset

3.5.1 Groundwater Level Measurements

Piezometric level data came from 190 observation wells sampled weekly, with only a few of them giving daily data. These observation wells are managed mainly by the APRONA (Association pour la PROtection de la Nappe d'Alsace) on the French side and by the LUBW-Baden-Württemberg (Landesanstalt für Umwelt, Messungen, und Naturschutz in Baden-Württemberg) on the German side. In this case study, the fluctuation of groundwater level is limited to less than few meters.

3.5.2 ESA CCI Microwave Soil Moisture

The ESA's (European Space Agency's) CCI program (Climate Change Initiative) provides soil moisture (SM) data from 1978 and on a spatial resolution of 0.25°. The CCI-SM data is the daily soil moisture for the top milli/centimeters of the soil. The CCI-SM version 05.2 uses microwave wavelengths to obtain soil moisture data using data from several sensors (Dorigo et al., 2017; http://www.esaoilmoisture-cci.org). CCI-SM uses passive microwave measurements (i.e., DMSP SSM/I, TRMM TMI, Aqua AMSR-E, Coriolis WindSat, SMOS, and SMAP). On the other hand, active data products are obtained using scatter meters in the C-band, which are installed on ERS-1, ERS-2, and ASCAT A-B satellites (Wagner et al., 2013). Cumulative density function matching was used to rescale the absolute soil moisture. For this purpose, the 0.25° resolution land surface soil moisture modeled data were used as a reference (GLDAS-NOAH, Rodell et al., 2004). In addition, both passive and active soil moisture products are merged herein, which was better than either one alone (Liu et al., 2011). Resampling and regridding to the target resolution of 0.0275° were done on the SM values in order to match the spatial resolution. This was done via the conservative interpolation of first-order (Jones, 1999). In this technique, the interpolation

weights are based on the fractional area overlap of the source and destination grid cells. The regridding in the conservative scheme allows for the preservation of flux fields of physical quantities between both the destination and source grids. The CCI-SM data reveal significant data gaps over the Upper Rhine Basin in all seasons. In the time period of 2012-2014, the temporal coverage (i.e., the ratio between the number of days with valid data and the number of total days) ranged from less than 10% (southern regions) to over 60% (northern regions) in Fig. 5. Finally, Fig. 6 shows the overall scheme of this study, which was given in the methods and data section.

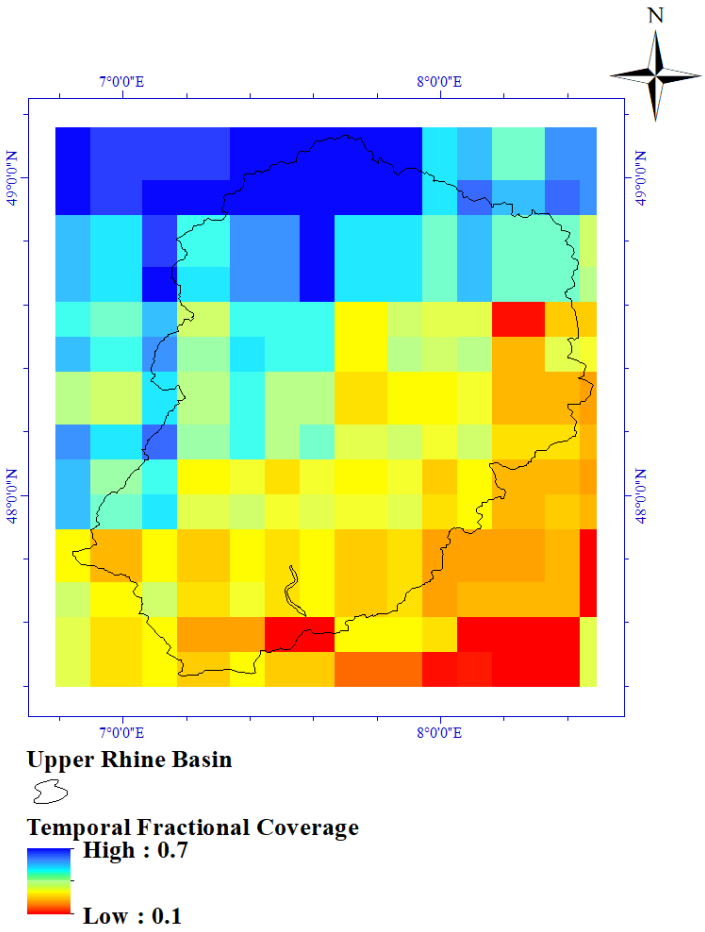

Fig. 5 Fraction of days that ESA-CCI SM data was reported over the time period of 2012-2014.

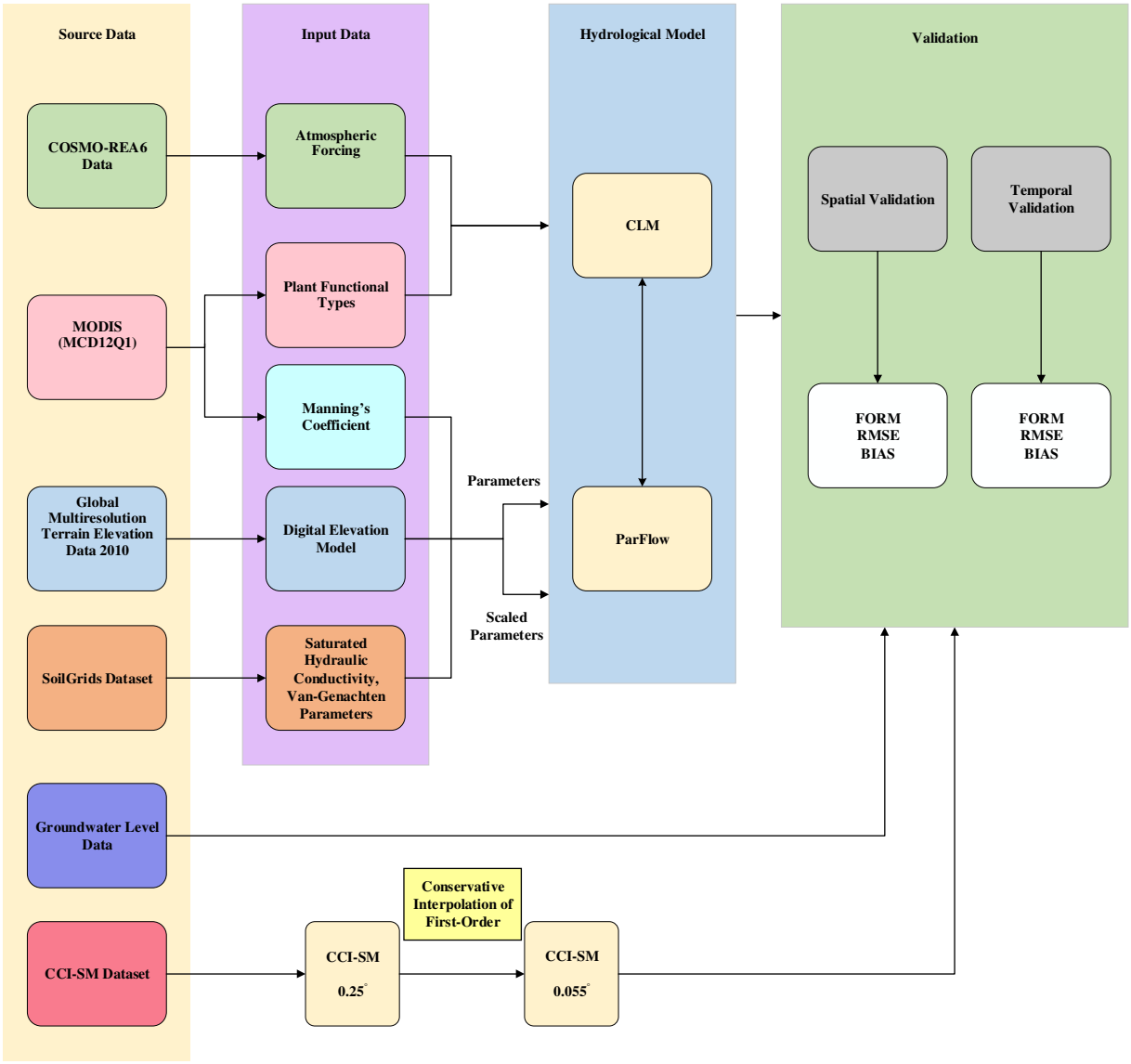

483

484 Fig. 6 Overall scheme of this study. Overall scheme to identify the used land surface and atmospheric
485 forcing, methodology of research and validation. Abbreviations: RMSE, root-mean-square deviation;
486 FORM, first order reliability method.

4. Results

4.1 Evaluation of Soil Moisture

4.1.1 Seasonal Mean Comparison

The seasonal volumetric soil water content (SWC) (mm^3/mm^3) from ParFlow-CLM without parameter scaling (ParFlow-CLM) and ParFlow-CLM with n and K_{Sat} scaling (ParFlow-CLM-S) is shown in Fig. 7, compared with the seasonal mean CCI-SM data.

In general, the ParFlow-CLM simulation has a higher SWC in all seasons (DJF, MAM, JJA, and SON) over most parts of the Upper Rhine Basin compared with the ParFlow-CLM-S simulation.

When comparing the ParFlow-CLM-S simulations with the CCI-SM observations, the spatial distribution of SWC in summer and autumn is better represented in the ParFlow-CLM-S simulations than in the ParFlow-CLM simulations (Fig. 7). Naz et al. (2018) assimilated the CCI-SM data into CLM to improve soil moisture and runoff simulations. The assimilation results showed a slightly better agreement with the CCI-SM data in the summer and autumn seasons than the spring and winter seasons. In this regard, data assimilation and n and K_{Sat} scaling improve soil moisture simulations in similar seasonal patterns.

For the time period of 2012-2014, Fig. 8 compares the temporally averaged SWC simulated by ParFlow-CLM and ParFlow-CLM-S to the CCI-SM data over the Upper Rhine Basin. In general, the SWC values were overestimated by ParFlow-CLM in all seasons. This overestimation was decreased with scaled n and K_{Sat}, as shown using ParFlow-CLM-S. It is worthy of note that the narrow spread of quartiles of the ParFlow-CLM-S-calculated SWC compared with the ParFlow-CLM in Fig. 8 indicates that scaling of n and K_{Sat} did not diminish spatial variability. Similarly, when validating models with CCI-SM data, the ParFlow-CLM improvements vary depending on the season. However, improvements were more noticeable for all seasons.

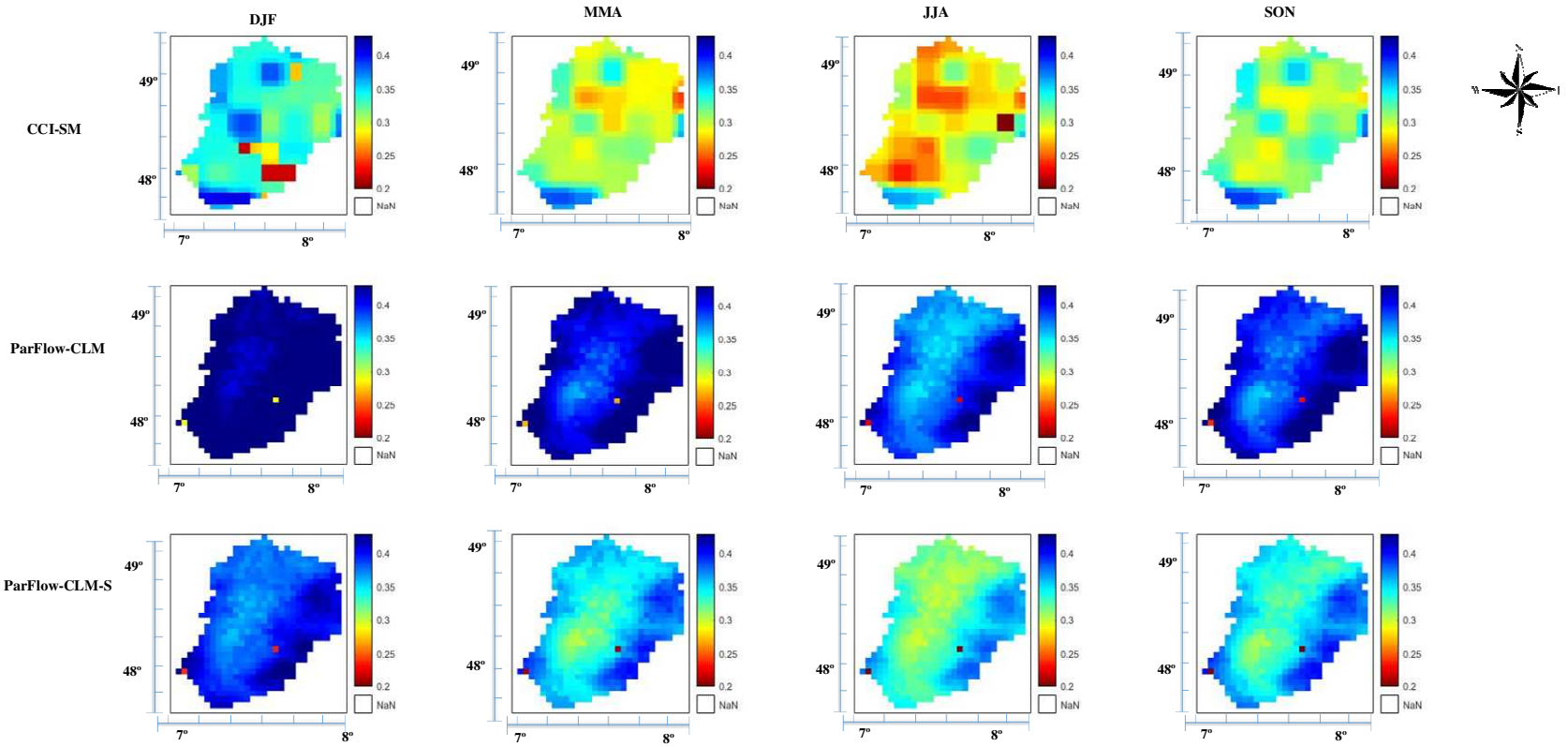

Fig. 7 Seasonally averaged SM simulated by ParFlow-CLM and ParFlow-CLM-S for the upper soil layer (0-5 cm) and compared to CCI-SM data for the DJF (December, January, and February), MAM (March, April, May), JJA (June, July, and August), and SON (September, October, and November) seasons from 2012 to 2014.

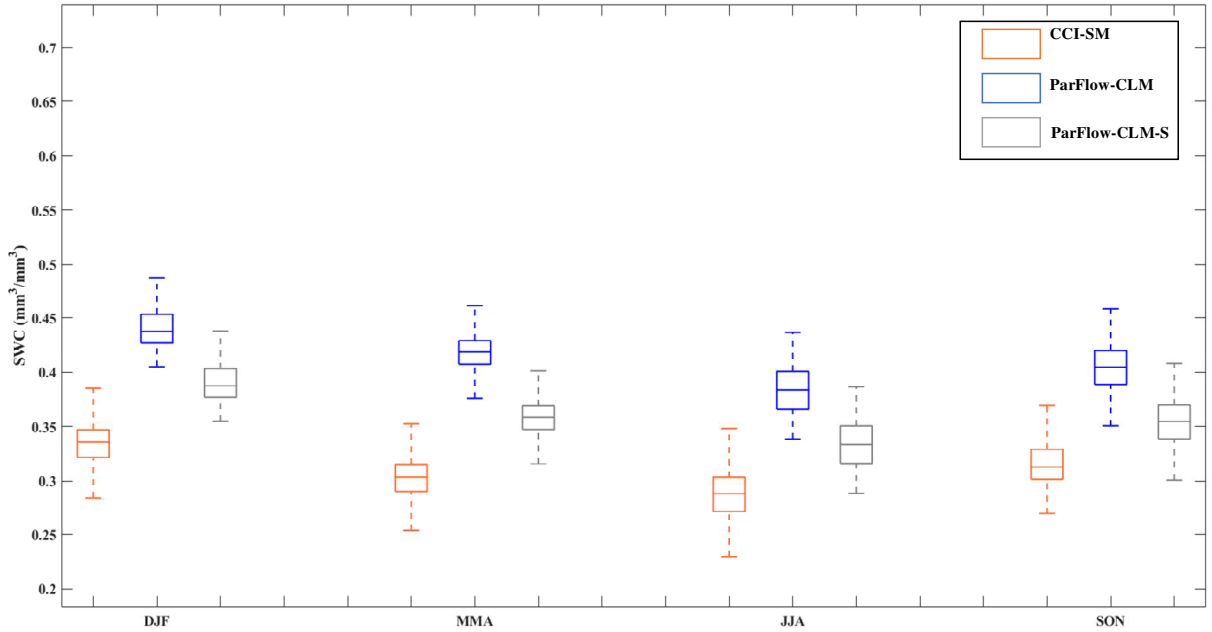

516

517 Fig. 8 Boxplot of seasonally averaged SWC simulated by ParFlow-CLM, ParFlow-CLM-S, and CCI-SM data from 2012 to 2014. DJF
518 (December, January, and February) represents winter; MAM (March, April, May) represents spring; JJA (June, July, and August)
519 represents summer and SON (September, October, and November) represents autumn. The central, bottom, and top marks on each box
520 represent the median and extreme values, respectively.

521 Cross-validation with CCI-SM observations was undertaken to assess the skill of ParFlow-CLM-S relative to ParFlow-CLM, and the
522 root mean square error (RMSE) and BIAS for soil moisture were calculated using daily values for the Upper Rhine Basin and all
523 seasons, as shown in Fig. 9. Note that the model data were only utilized to calculate these statistics on days when satellite data were
524 available. For all seasons in the Upper Rhine Basin, ParFlow-CLM-S had a consistently lower RMSE than ParFlow-CLM, with the
525 exception of winter, when the SWC benefits were relatively minor (Fig. 9 c and d).

For all regions, the mean RMSE decreased from 0.03 mm^3/mm^3 (ParFlow-CLM) to 0.005 mm^3/mm^3 (ParFlow-CLM-S). The BIAS shows a substantial overestimation of soil moisture in comparison to the satellite CCI-SM observations (Fig. 9 a and b), while the BIAS for soil moisture from ParFlow-CLM-S is considerably decreased (Fig. 9 a and b). For all regions, the mean BIAS decreased from 0. 17 mm^3/mm^3 (ParFlow-CLM) to 0. 1 mm^3/mm^3 (ParFlow-CLM-S). In addition, an innovative implementation of the FORM is used to examine the LSF failure probability as a criterion for verifying the model's results closure. By defining r less than 0.25, r can be used as a criterion to assess the reliability of the model's results.

To this end, the first-order reliability method finds failure probability (P_f) of the model's results closure. Table 2 shows the results of the FORM implementation for soil moisture simulations of ParFlow-CLM and ParFlow-CLM-S over all seasons. Since P_f in ParFlow-CLM-S is lower than ParFlow-CLM, the closure and consistency of the model's results using the scaling approach are acceptable. The FORM results show that the probability of a substantial divergence between the ParFlow-CLM-S soil moisture results and the CCI-SM observation, which is defined as more than 0.25% of the CCI-SM observation value, is 0.05, 0.11,0.15, and 0.08 for autumn, winter, spring, and summer, respectively. The failure probability of the defined LSF in winter is a little more than that of the other seasons.

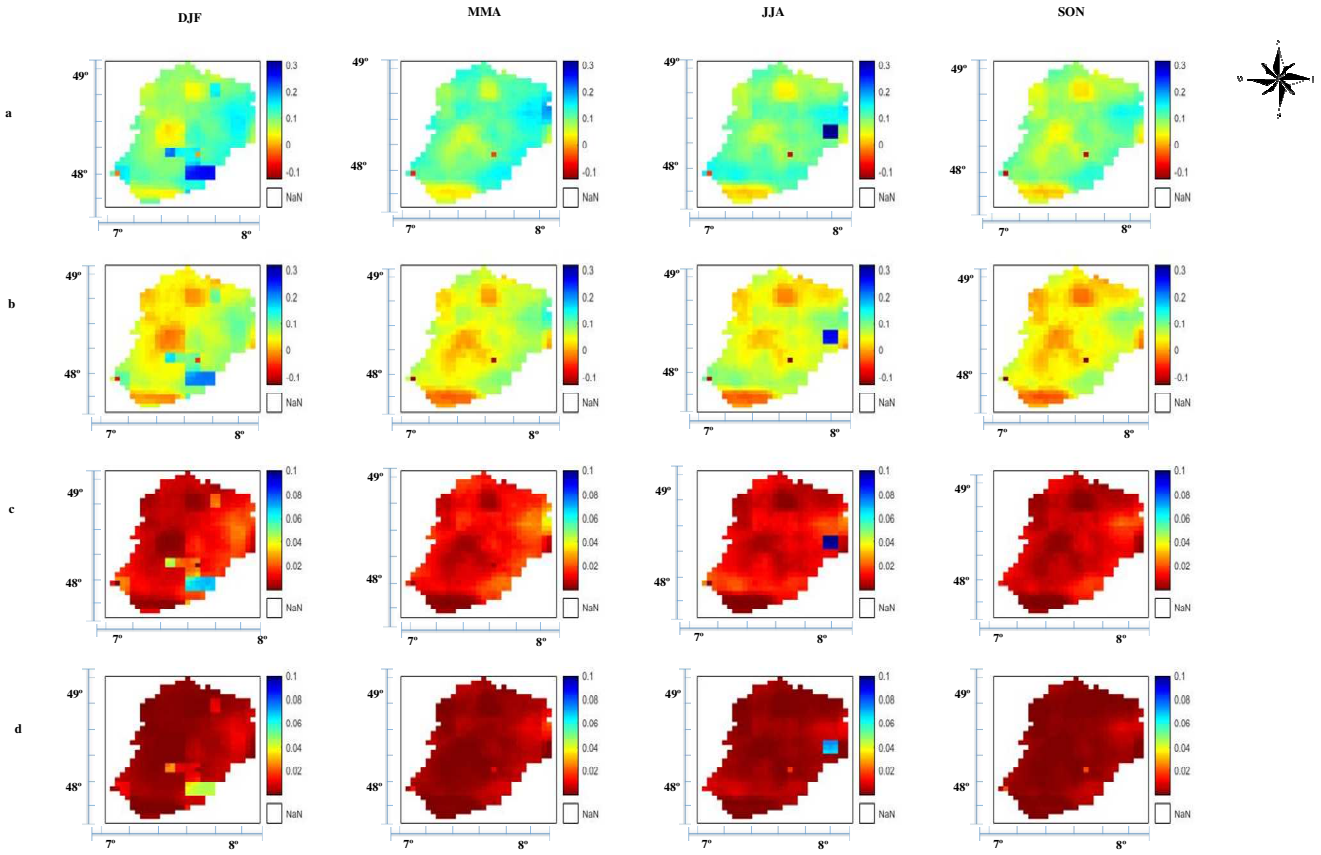

Fig. 9 RMSE and BIAS for daily soil water content for the DJF (December, January, and February), MAM (March, April, May), JJA (June, July, and August), and SON (September, October, and November) seasons from 2012 to 2014. (a) BIAS for ParFlow-CLM and (b) BIAS for ParFlow-CLM-S (c) RMSE for ParFlow-CLM and (d) RMSE for ParFlow-CLM-S simulations over the years 2012-2014.

545 Table 2. The results of FORM implementation for soil moisture simulations of ParFlow-CLM
546 and ParFlow-CLM-S over DJF (December, January, and February), MAM (March, April, May),
547 JJA (June, July, and August), and SON (September, October, and November).

Months	P_f	
	ParFlow-CLM-S	ParFlow-CLM
SON	0.15	0.05
DJF	0.25	0.11
MMA	0.22	0.15
JJA	0.19	0.08

548

549 *4.1.2 Daily Validation*

550 The daily SM averaged from January 2012 to December 2014 over the Upper Rhine Basin (Fig.
551 10), as simulated by ParFlow-CLM and ParFlow-CLM-S and as observed by CCI-SM, is
552 presented in Fig. 10.

553 In ParFlow-CLM-S, the scaling approach improved the simulations of SWC. The daily SWC
554 patterns predicted by ParFlow-CLM-S are very similar to the CCI-SM data, with general
555 agreement across the basin.

556 When compared with the entire period, the CCI-SM observations show increased variability and
557 drier soil moisture values during the summer. In general, the daily soil moisture predicted by the
558 ParFlow-CLM-S agree with the CCI-SM data relatively better in the summer and autumn
559 seasons than in the spring and winter seasons.

Due to dense vegetation, frozen soil, and/or model errors associated to modeling soil moisture in colder climates, ParFlow-CLM-S performs worse in the winter season (Oleson et al., 2008).

For the time period 2012-2014, Table 3 compares some important statistical parameters, such as mean and variance of the spatially averaged soil moisture simulated by ParFlow-CLM and ParFlow-CLM-S, to the CCI-SM data over the Upper Rhine Basin. In general, the soil moisture of the first soil layer simulated by ParFlow-CLM is higher than the CCI-SM data in all seasons. This overestimation was decreased by using scaled n and K_{Sat}, as shown using ParFlow-CLM-S. It is worthy of note that the soil moisture simulated by ParFlow-CLM-S compared with ParFlow-CLM in Table 3 indicates that improvements were more noticeable for all seasons.

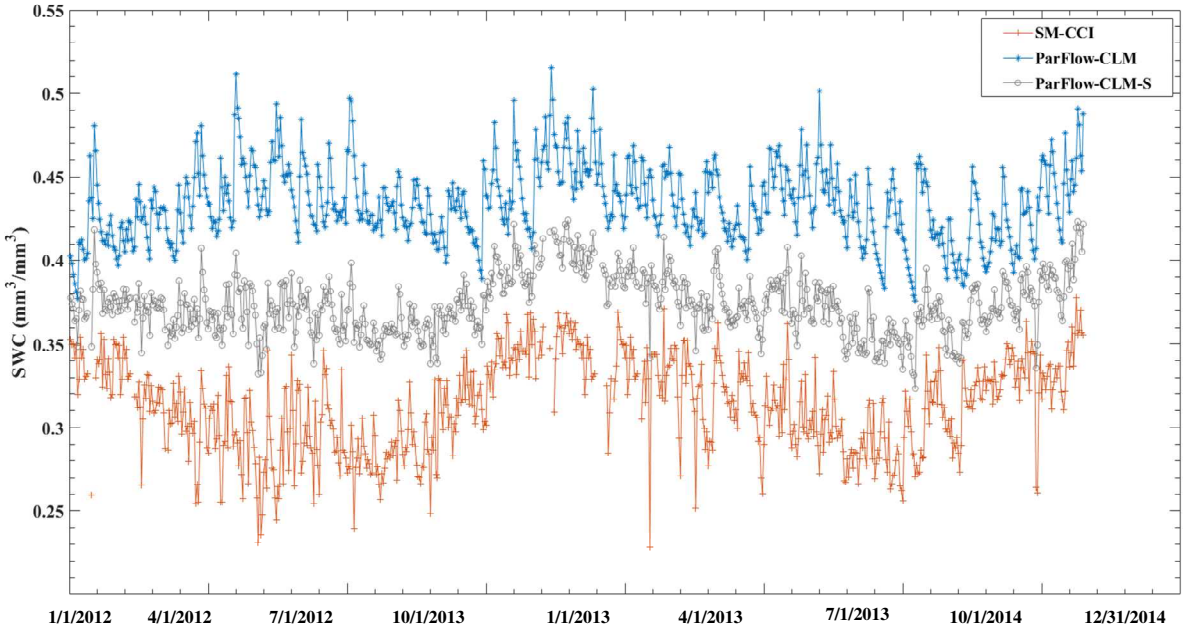

Fig. 10 Spatially averaged daily SWC simulated with ParFlow-CLM-S and ParFlow-CLM and compared to CCI-SM data for the Upper Rhine Basin from 2012 to 2014.

573 Table 3. Some statistical parameters for soil moisture simulations of ParFlow-CLM and
574 ParFlow-CLM-S and CCI-SM data for DJF (December, January, and February), MAM (March,
575 April, May), JJA (June, July, and August), and SON (September, October, and November).

Months	CCI-SM		ParFlow-CLM		ParFlow-CLM-S	
	Mean	**variance**	**Mean**	**variance**	**Mean**	**variance**
DJF	0.327	0.047	0.44	0.025	0.39	0.019
MMA	0.306	0.0253	0.417	0.022	0.357	0.02
JJA	0.288	0.033	0.354	0.027	0.334	0.023
SON	0.318	0.0247	0.384	0.023	0.354	0.023

576 *4.2 Evaluation of Groundwater Level: Annual mean comparison*

577 Fig. 11 shows the groundwater level estimates of ParFlow-CLM and ParFlow-CLM-S, compared
578 with the groundwater level (from sea level) from well observations. ParFlow-CLM simulates
579 higher magnitudes of groundwater level (on average 146 m) over most parts of the basin
580 compared with ParFlow-CLM-S (on average, 143 m).

581 The overestimation in the ParFlow-CLM simulations was more significant in the central regions
582 of the basin (Fig. 11). Compared with ParFlow-CLM, regional groundwater-level patterns
583 simulated by ParFlow-CLM-S agree better with groundwater-level observations. When
584 compared with well data in the central and northern regions of the basin, the ParFlow-CLM-S
585 performs better.

586 As shown in Fig. 11, the scaling approach clearly resulted in an overall improvement in the
587 simulated groundwater level for all regions.

588 Averaged annual groundwater level improvements are especially noticeable over the central and
589 northern regions, where ParFlow-CLM-S reduced the discrepancy between the well data and the

model's result, from 6 m to 3 m. The groundwater level from well observations was interpolated using the Kriging method (Krige, 1951). Some part of this difference is related to Kriging uncertainty. Several studies have addressed errors raised from uncertainty in random function estimation steps of the Kriging methodology (Loquin and Dubois, 2010; Lloyd and Atkinson, 2001). As a result, uncertainty of the used model by using scaled parameters in groundwater-level estimation is less than 3 m.

Where the groundwater table is not shallow (more than 5 meters), the improvements over other regions of the basin, such as the southern regions, were relatively small. These results highlight the potential of the scaling approach in improving shallow groundwater where the surface–subsurface coupling is most impactful.

The failure probability of LSF is investigated as a criterion to assess the reliability of the model's results by using a novel application of the First Order Reliability Method (FORM). By specifying r smaller than 0.1, it can be used as a criterion to assess the reliability of the model's results.

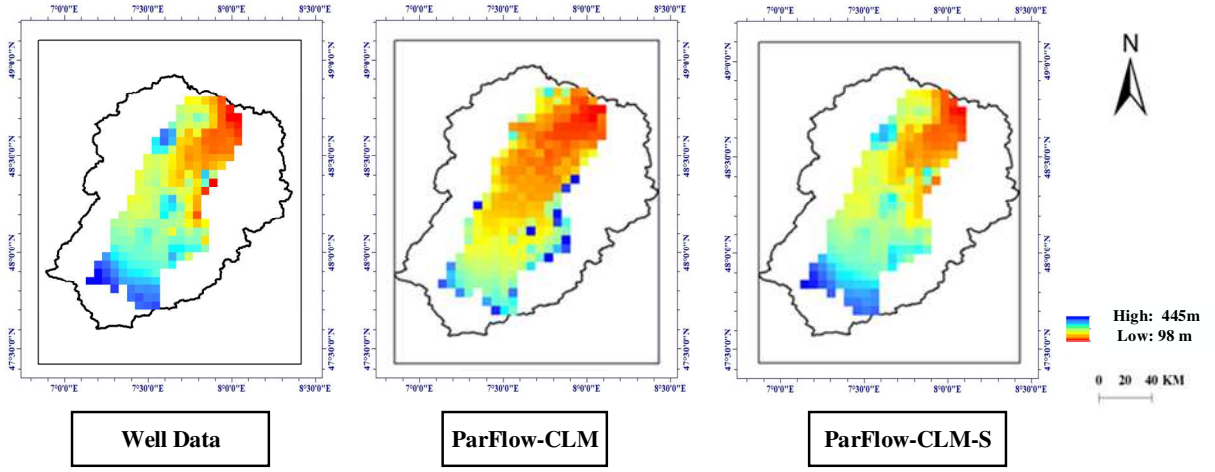

606

607 Fig. 11 Temporally averaged annual groundwater level from the sea level (m) simulated by
608 ParFlow-CLM and ParFlow-CLM-S for the years 2012 – 2014 over the Upper Rhine Graben.
609 Temporally averaged groundwater level from well data is shown for comparison.

610

611 To achieve this, the FORM calculates the failure probability (P_f) of the model's results closure.
612 The results of the FORM implementation show that the failure probability of simulated annual
613 groundwater level by ParFlow-CLM and ParFlow-CLM-S is 0.05 and 0.1, respectively. Since P_f
614 in ParFlow-CLM-S is lower than in ParFlow-CLM, the scaling approach is sufficiently accurate
615 for model closure and consistency.

616 For the time period 2012-2014, Table 4 compares some important statistical parameters, such as
617 the mean, maximum, and minimum of the temporally averaged groundwater level simulated by
618 ParFlow-CLM and ParFlow-CLM-S to the well data over the Upper Rhine Basin.

619 In general, the groundwater-level values (from the sea level) decreased by the ParFlow-CLM in
620 all seasons. This overestimation was decreased with scaled n and K_{Sat}, as shown using ParFlow-
621 CLM-S, because groundwater level is closed to the surface. It is worthy of note that the
622 groundwater level simulated by ParFlow-CLM-S compared with ParFlow-CLM in Table 4

623 indicates that scaling of n and K_{Sat} did not diminish the spatial variability. Improvements were
624 more noticeable for all seasons.

625 Table 4. Some statistical parameters for groundwater-level simulations of ParFlow-CLM and
626 ParFlow-CLM-S and well data for DJF (December, January, and February), MAM (March,
627 April, May), JJA (June, July, and August), and SON (September, October, and November).

Months	Well data			ParFlow-CLM-S			ParFlow-CLM		
	Mean	**Max**	**Min**	**Mean**	**Max**	**Min**	**Mean**	**Max**	**Min**
DJF	165.1	708.64	99.98	170.3	713.84	105.18	175.1	718.64	109.98
MMA	163.6	708.01	99.26	168.4	712.81	104.06	171.7	716.11	107.36
JJA	163.09	707.95	99.78	166.99	711.85	103.68	169.89	714.75	106.58
SON	164.46	708.86	99.84	168.96	713.36	104.34	173.46	717.86	108.84

628

629 Fig. 12 depicts a weekly groundwater-level time series that shows that ParFlow-CLM greatly
630 overestimates the magnitude of the groundwater level. Over all regions, the ParFlow-CLM-S
631 decreases these biases, and the groundwater-level simulations with ParFlow-CLM-S are more
632 consistent with the well observations. Certainly, better agreement with the observations would be
633 obtained with the real soil characteristics for layers deeper than 2 m. This improvement would be
634 observed not only with the results of the new model, based on the scaling approach, but also on
635 the results of the standard model (i.e., without the scaling approach).

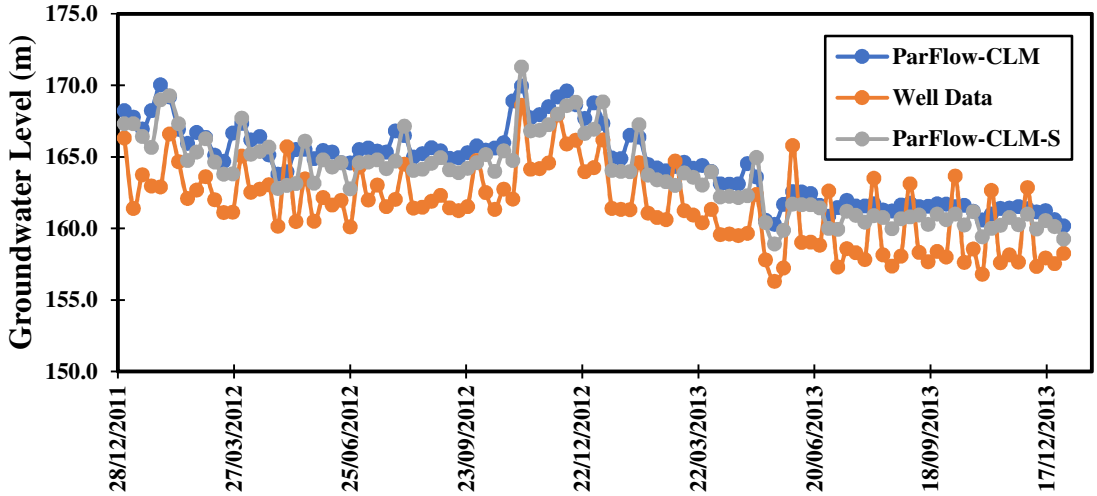

636

637 Fig. 12 Spatially averaged weekly groundwater levels simulated with ParFlow-CLM-S and
638 ParFlow-CLM and compared to CCI-SM data for the Upper Rhine Basin from 2012 to 2014.

639 **5. Discussion**

640 The hydrologic community is particularly interested in continental-scale hydrologic simulations
641 for a variety of socioeconomic, scientific, and practical reasons. Condon et al. (2015) and
642 Condon and Maxwell (2017) used the coupled hydrology-land surface model ParFlow-CLM
643 configured to investigate scale-dependent connections between water table depth, topography,
644 recharge, and evapotranspiration, as well as the effects of anthropogenic aquifer depletion on the
645 water and energy balance. These studies have enabled for a high-resolution and process-based
646 knowledge of the continental water cycle.

647 O'Neill et al. (2020) conducted the most extensive review of ParFlow-CLM performance to date
648 over the continental United States, comparing thousands of in situ observations and many remote
649 sensing products with a variety of statistical performance indicators. Comparisons of ParFlow-

650 CLM with these datasets show that the model is dependable and capable of accurately
651 reproducing the continental-scale water balance at high resolution.

652 This study and some other recent studies (e.g., Koch et al., 2016; Gebler et al., 2017) highlight
653 the capabilities of the coupled ParFlow-CLM model in studying different water budget
654 components or hydrologic fluxes. Koch et al. (2016) have studied the performance of the
655 ParFlow-CLM model, compared with other models such as the HydroGeoSphere (Panday and
656 Huyakorn, 2004; Therrien et al., 2010) and MIKE SHE (Abbott et al., 1986; Graham and Butts,
657 2005) for estimation of soil moisture. ParFlow-CLM provided a more accurate prediction of soil
658 moisture in terms of temporal dynamics and heterogeneity at the catchment scale. The
659 HydroGeoSphere and MIKE SHE models delivered more detailed soil moisture estimates at the
660 local scale. Generally, their findings showed that topography is one of the key influential factors
661 on soil moisture variability which have overemphasized feedback in ParFlow-CLM.

662 Gebler et al. (2017) evaluated the effect of different soil hydraulic parametrization methods in
663 the ParFlow-CLM model and showed that the variability in soil hydraulic parameters, rather than
664 topography or other causes of variability, dominates spatial variability in soil moisture content at
665 the subcatchment scale.

666 Foster and Maxwell (2019) have proposed a scaling method for effective hydraulic conductivity
667 and Manning's coefficient to compensate for the loss of topographic gradients in coarse
668 resolution simulations. In this study, simulations have been done using different hydraulic
669 conductivity over four orders of magnitude in a real case study at 1-km and 100-m resolution.
670 These findings indicate that, when simulations are done at a coarse resolution, effective
671 hydraulic conductivity must be biased higher. This study is in a good agreement with our

672 findings and shows that scaling of hydraulic properties, such as hydraulic conductivity,
673 obviously improves the results of the ParFlow-CLM model in less resolution simulations.

674 Other studies have also applied different hydrological models to estimate groundwater level in
675 the Rhine-Meuse Basin. Sutanudjaja et al. (2011) used a MODFLOW transient groundwater
676 model, which was forced to recharge, and the surface water level, which was calculated by the
677 land surface model. Absolute mean bias for some parts of the basin is higher than 50 m, while
678 the maximum absolute mean bias is lower than 3 m in our study. This can be attributed to the use
679 of an offline coupling technique in MODFLLOW that oversimplifies the dynamic feedback
680 between surface water and groundwater loads, and between the moisture state of soil and the
681 groundwater level. In the coupled ParFlow-CLM approach, the interaction between surface and
682 subsurface is more suitable for the case study. It could also be due to differences in model
683 parameters and calibration.

684 Considering the model calibration, several studies investigated methods to improve the
685 hydrological models' predictions. Sutanudjaja et al. (2014) have investigated the possibility of
686 calibrating the PCRaster Global Water Balance (PCR-GLOBWB) (Van Beek & Bierkens, 2009),
687 which is coupled with the MODFLOW (McDonald and Harbaugh, 1988) (PCR-GLOBWB-
688 MOD) model (Sutanudjaja et al., 2011), by using remotely sensed soil moisture data and in situ
689 runoff observations. Calibration is performed by executing the model 3045 times with various
690 parameter values that affect the dynamics of the groundwater level in the Rhine-Meuse Basin. In
691 this work, the scaling approach is used without calibration. It shows better agreement with
692 observations than the standard model (i.e., without the scaling approach). Thus, this approach
693 will better reproduce the observations when it is used for model calibration. In order to improve
694 model performance, Tangdamrongsub et al. (2015) have assimilated total water storage (TWS)

695 data obtained from the Gravity Recovery and Climate Experiment (GRACE) data into the
696 OpenStreams wflow-hbv model, which is a distributed version of the HBV-96 model
697 (Schellekens, 2014), using an ensemble Kalman filter (EnKF) method over the Rhine River
698 basin. Although their results highlighted the benefit of assimilating GRACE data into
699 hydrological models, they could be improved if limitations such as the lack of sufficient
700 constraints on the soil moisture component did not exist. In the current implementation of
701 ParFlow-CLM-S, the enhancement did not rely on the use of additional spatial information, but
702 on the better parametrization and scale change, which renders it robust, as the inaccessibility to a
703 specific dataset does not affect the results. Nevertheless, it would be of interest to test whether
704 the combined use of scale change and earth observation data would yield better predictions or a
705 reduction of uncertainties.

706 Selecting the threshold value for effective width affects the number of cells used in the scaling
707 process. If a large threshold value is considered for the effective width, the number of cells for
708 which the scaling process is performed will decrease, and if threshold value is small, the number
709 of these cells will increase. Depending on the climatic conditions of the study area and the
710 density of the river network, the simulation time period, and the resolution of the model, the
711 effect of the threshold value on the model simulation results changes. For example, if the study
712 area has an arid or semi-arid climate that has been experiencing drought for a long time or a
713 seasonal river is flowing in the study area at a specific time of year, more care should be taken to
714 select the threshold value. Therefore, if a low threshold value is considered, the scaling process
715 is performed for a period when the river is not flowing and thus affects the model simulation
716 results. This is also important for regions that experience severe flooding during a specific time

period. In these areas, if the threshold value is considered high, the number of pixels used during the flood and wet season decreases and influences the model simulation results.

There is no certain criterion for choosing this low limit; however, it is suggested that rivers that do not exist in more than 50% of the simulation time period and flow for a short time due to floods and seasonal variations in rainfall should not be considered in scaling operations. According to Schalge et al.'s (2019) study, model resolution is one of the most critical factors, and the success of the scaling process decreases when the river width is less than 1/10th of the model resolution. However, our findings show that the success of the scaling process is acceptable even if the width of the rivers is less than 1/10th of the model resolution. It might be related to the high density of the river network in our case study, which exchanged much water between the surface and the subsurface. In this regard, it is suggested that a comprehensive study be done to investigate the effect of model resolution and the river network density on the performance and accuracy of the scaling process.

In this study, we used an integrated ParFlow-CLM model, which is physics based and requires the many input data listed in Table 1. Calibration of these models, unlike concept models, due to the huge computational cost, is not widely used. Only the two parameters (porosity and specific storage) should be evaluated when the scaling approach is used for calibration. If the number of these scenarios is high, the computational load will increase significantly. However, a calibration with a limited number of scenarios may help to improve the results.

6. Summary and Conclusions

We suggested an approach to improve soil moisture and groundwater-level predictions from a distributed hydrological model using an objective scaling of Manning's coefficient and saturated

739 hydraulic conductivity. This approach was applied for the Upper Rhine Basin at approximately a
740 6-km resolution for the years 2012 to 2014. Since the interaction between the surface and
741 subsurface is significant in this case study, because of the presence of shallow aquifers, an
742 integrated surface–subsurface model, ParFlow, was used. ParFlow is a grid-scale model that
743 calculates overland flow at a constant horizontal grid resolution and employs the kinematic wave
744 approximation for both hillslope and river channel flow. Since the width of rivers is much
745 narrower than the grid size of the model, the exchange between the river and subsurface is
746 approximated as higher than realistic rivers, resulting in an erroneously large
747 infiltration/exfiltration rate. The scaling parameters approach is used to compensate for this
748 limitation. The impact of the scaling approach on the soil moisture and groundwater level was
749 evaluated and cross-validated with the CCI-SM data and the groundwater-level data from well
750 observations at seasonal scales. Furthermore, the reliability of the used scaling approach was
751 examined by a novel probabilistic framework (FORM). Using this scaling approach, the
752 conclusions of this study are as follows.

753 1. This study showed that scaling of Manning's coefficient and saturated hydraulic conductivity
754 improved the soil moisture simulations and groundwater level over most parts of the Upper
755 Rhine Basin relative to the model's simulations without parameter scaling. The ParFlow-CLM
756 simulations overestimated the SM in most parts of the Upper Rhine Basin and in all seasons.
757 Major improvements in the groundwater level have been made over most of the basin's regions,
758 particularly in the central and northern regions. Our simulation results of ParFlow-CLM and
759 ParFlow-CLM-S in these regions may show that scaling is more successful in a shallow
760 groundwater simulation. The average bias in soil moisture for the study domain was decreased

761 from 0.017 mm^3/mm^3 in ParFlow-CLM simulations to 0.01 mm^3/mm^3 in ParFlow-CLM-S
762 simulations.

763 2. The ParFlow-CLM-S soil moisture simulations performed better in the summer and autumn
764 seasons than in the winter and spring seasons on a seasonal time scale. The FORM results show
765 that the accuracy of the ParFlow-CLM soil moisture simulations by using scaling approach is
766 more than 0.05, 0.11, 015, and 0.08 for autumn, winter, spring and summer, respectively.

767 The ParFlow-CLM model simulations of soil moisture and groundwater level over the Upper
768 Rhine Basin benefit from scaling of Manning's coefficient and saturated hydraulic conductivity,
769 as demonstrated in this work. However, there are a few limitations in this research. The spatial
770 mismatch between our high-resolution land surface model and the coarser resolution CCI-SM
771 was addressed by rescaling the CCI-SM data to the model resolution (6 km) without bias
772 correction. In addition to inconsistencies at the spatial scale, data gaps in satellite soil moisture
773 retrievals, which are limited in regions of pronounced topography, standing water, dense
774 vegetation, snow-covered areas, and frozen soil, can cause inaccuracies in soil moisture
775 estimations (Dorigo et al., 2017).

776 When the width of a river is known with adequate accuracy, this concept can simply be used in
777 all models that do not explicitly resolve the true river width for river routing. Only a preparation
778 step is necessary in practice, which does not add to the computational load during runtime. No
779 equivalent solutions have been tried to our knowledge because most approaches rely on
780 dedicated channel parametrizations, which are far more difficult to implement. Finally, the
781 results indicate that a modification of model parametrization to take into account the impact of
782 scale on hydrodynamic parameters should be done prior to multivariate assimilation approaches.
783 The current work investigates the effect of the scaling approach on soil moisture and

784 groundwater budget. Future extensions of this work could include the effect of the scaling
785 approach on stream discharge.

786 **Acknowledgements**

787 Support from the Research Office of the Sharif University of Technology, Iran, is acknowledged.
788 We also thank the anonymous reviewers for providing constructive comments on the manuscript.
789 Thank you for your comments and suggestions that allowed us to greatly improve the quality of
790 the manuscript.

791 **Reference**

792 Ababou, R. et al., 2015. Model coupling for environmental flows, with applications in hydrology
793 and coastal hydrodynamics. (2): 9-24.

794 Abbott, M., Bathurst, J., Cunge, J., O'connell, P., Rasmussen, J., 1986. An introduction to the
795 European Hydrological System—Systeme Hydrologique Europeen, "SHE", 2: Structure of a
796 physically-based, distributed modelling system. Journal of hydrology, 87(1-2): 61-77.

797 Abdelkhalak, E.H., Bouchaïb, R., 2013. Incertitudes, optimisation et fiabilité des structures.
798 Lavoisier.

799 Ajami, H., McCabe, M.F., Evans, J.P., Stisen, S., 2014. Assessing the impact of model spin-up
800 on surface water-groundwater interactions using an integrated hydrologic model. Water
801 Resources Research, 50(3): 2636-2656.

802 Asante, K.O., Artan, G.A., Pervez, S., Bandaragoda, C., Verdin, J.P.J.W.W.W., 2008. Technical
803 manual for the geospatial stream flow model (GeoSFM). 605: 594-6151.

804 Ashby, S. F. and Falgout, R. D.: A Parallel Multigrid Preconditioned Conjugate Gradient
805 Algorithm for Groundwater Flow Simulations, Nucl. Sci. Eng., 124, 145–159, 1996.

806 Batjes, N.J.S.u., management, 1997. A world dataset of derived soil properties by FAO–
807 UNESCO soil unit for global modelling. 13(1): 9-16.

808 Beisman, J., 2007. Development of a parallel reactive transport model with spatially variable
809 nitrate reduction in a floodplain aquifer, A thesis submitted to the Faculty and the Board of
810 Trustees of the Colorado School of Mines in partial fulfillment of the requirements for the degree
811 of Master of Science (Hydrology).

812 Bollmeyer, C. et al., 2015. Towards a high-resolution regional reanalysis for the European
813 CORDEX domain. 141(686): 1-15.

814 Christiansen, L. et al., 2007. Local to regional hydrological model calibration for the Okavango
815 River basin from in-situ and space borne gravity observations, Proceedings of 2nd Space for
816 Hydrology Workshop, Geneva, Switzerland, 12-14 November 2007.

817 Clark, M.P. et al., 2015. Improving the representation of hydrologic processes in Earth System
818 Models. 51(8): 5929-5956.

819 Condon, L.E., Hering, A.S., Maxwell, R.M., 2015. Quantitative assessment of groundwater
820 controls across major US river basins using a multi-model regression algorithm. Advances in
821 Water Resources, 82: 106-123.

822 Condon, L.E., Maxwell, R.M., 2017. Systematic shifts in Budyko relationships caused by
823 groundwater storage changes. Hydrology and Earth System Sciences, 21(2): 1117-1135.

824 Dai, Y. et al., 2003. Oleson., KW, Schlosser, CA, and Yang, Z.: the common land model. Bull.
825 Am. Meteorol. Soc, 84: 1013-1023.

826 Danielson, J.J., Gesch, D.B., 2011. Global multi-resolution terrain elevation data 2010
827 (GMTED2010). US Department of the Interior, US Geological Survey.

828 Decharme, B. et al., 2012. Global off-line evaluation of the ISBA-TRIP flood model. Climate
829 Dynamics, 38(7): 1389-1412.

830 Dorigo, W. et al., 2017. ESA CCI Soil Moisture for improved Earth system understanding: State-
831 of-the art and future directions. 203: 185-215.

832 Döll, P., Kaspar, F., Lehner, B.J.J.o.H., 2003. A global hydrological model for deriving water
833 availability indicators: model tuning and validation. 270(1-2): 105-134.

834 Eagleson, P.S., 1978. Climate, soil, and vegetation: 1. Introduction to water balance dynamics.
835 Water Resources Research, 14(5): 705-712.

836 Engdahl, N.B., McCallum, J.L., Massoudieh, A.J.J.o.H., 2016. Transient age distributions in
837 subsurface hydrologic systems. 543: 88-100.

838 Ferguson, I.M., Maxwell, R.M.J.E.R.L., 2012. Human impacts on terrestrial hydrology: climate
839 change versus pumping and irrigation. 7(4): 044022.

840 M. Foster, L., M. Maxwell, R., 2019. Sensitivity analysis of hydraulic conductivity and
841 Manning's n parameters lead to new method to scale effective hydraulic conductivity across
842 model resolutions. Hydrological Processes, 33(3): 332-349.

843 Friedl, M.A. et al., 2002. Global land cover mapping from MODIS: algorithms and early results.
844 83(1-2): 287-302.

845 Gebler, S., Franssen, H.-J.H., Kollet, S., Qu, W., Vereecken, H., 2017. High resolution
846 modelling of soil moisture patterns with TerrSysMP: A comparison with sensor network data.
847 Journal of hydrology, 547: 309-331.

848 Graham, D.N., Butts, M.B., 2005. Flexible, integrated watershed modelling with MIKE SHE.
849 Watershed models, 849336090: 245-272.

850 Gutowski Jr, W.J. et al., 2016. WCRP coordinated regional downscaling experiment
851 (CORDEX): a diagnostic MIP for CMIP6. 9(11): 4087-4095.

852 Hengl, T. et al., 2017. SoilGrids250m: Global gridded soil information based on machine
853 learning. 12(2): e0169748.

854 Huang, S. et al., 2017. Evaluation of an ensemble of regional hydrological models in 12 large-
855 scale river basins worldwide. 141(3): 381-397.

856 Jones, P.W.J.M.W.R., 1999. First-and second-order conservative remapping schemes for grids in
857 spherical coordinates. 127(9): 2204-2210.

858 Jones, J.E., Woodward, C.S.J.A.i.W.R., 2001. Newton–Krylov-multigrid solvers for large-scale,
859 highly heterogeneous, variably saturated flow problems. 24(7): 763-774.

860 Koch, J. et al., 2016. Inter-comparison of three distributed hydrological models with respect to seasonal
861 variability of soil moisture patterns at a small forested catchment. Journal of hydrology, 533: 234-249.

862 Kollet, S.J., Maxwell, R.M.J.A.i.W.R., 2006. Integrated surface–groundwater flow modeling: A
863 free-surface overland flow boundary condition in a parallel groundwater flow model. 29(7): 945-
864 958.

865 Kollet, S.J., Maxwell, R.M., 2008. Capturing the influence of groundwater dynamics on land
866 surface processes using an integrated, distributed watershed model. Water Resources Research,
867 44(2).

868 Koltzer, N., Scheck-Wenderoth, M., Cacace, M., Frick, M., Bott, J., 2019. Regional hydraulic
869 model of the Upper Rhine Graben. Advances in Geosciences, 49: 197-206.

870 Krige, D.G.J.J.o.t.S.A.I.o.M., Metallurgy, 1951. A statistical approach to some basic mine
871 valuation problems on the Witwatersrand. 52(6): 119-139.

872 Kuffour, B. N. O.: Parflow-350/parflow: ParFlow Version 3.5.0, Zenodo,
873 https://doi.org/10.5281/zenodo.3555297, 2019.

874 Kuffour, B.N. et al., 2020. Simulating coupled surface–subsurface flows with ParFlow v3. 5.0:
875 capabilities, applications, and ongoing development of an open-source, massively parallel,
876 integrated hydrologic model. 13(3): 1373-1397.

877 Liu, Y.Y. et al., 2011. Developing an improved soil moisture dataset by blending passive and
878 active microwave satellite-based retrievals. 15(2): 425-436.

879 Lloyd, C., Atkinson, P.M.J.C., Geosciences, 2001. Assessing uncertainty in estimates with
880 ordinary and indicator kriging. 27(8): 929-937.

881 Loquin, K., Dubois, D., 2010. Kriging and epistemic uncertainty: a critical discussion, Methods
882 for Handling Imperfect Spatial Information. Springer, pp. 269-305.

883 McDonald, M.G., Harbaugh, A.W., 1988. A modular three-dimensional finite-difference ground-
884 water flow model. US Geological Survey.

885 Madsen, H.O., Krenk, S., Lind, N.C., 2006. Methods of structural safety. Courier Corporation.

886 Majdalani, S., Ackerer, P.J.G., 2011. Identification of groundwater parameters using an
887 adaptative multiscale method. 49(4): 548-559.

888 Maxwell, R. M.: A terrain-following grid transform and preconditioner for parallel, large-scale,
889 integrated hydrologic modeling, Adv. Water Resour., 53, 109–117,
890 https://doi.org/10.1016/j.advwatres.2012.10.001, 2013.

891 Maxwell, R., Condon, L., Kollet, S.J.G.m.d., 2015. A high-resolution simulation of groundwater
892 and surface water over most of the continental US with the integrated hydrologic model ParFlow
893 v3. 8(3): 923-937.

894 Maxwell, R.M. et al., 2009. ParFlow user's manual. 1(2009): 129.

895 Maxwell, R.M. et al., 2011. Development of a coupled groundwater–atmosphere model. 139(1):
896 96-116.

897 Maxwell, R. M. and Miller, N. L.: Development of a Coupled Land Surface and Groundwater
898 Model, J. Hydrometeorol., 6, 233–247, https://doi.org/10.1175/JHM422.1, 2005.

899 Nataf, A.J.C.R.d.l.A.d.S., 1962. Determination des distribution don t les marges sont donnees.
900 225: 42-43.

901 Naz, B.S. et al., 2018. Improving soil moisture and runoff simulations over Europe using a high-
902 resolution data-assimilation modeling framework. 1(FZJ-2018-03144): 1-32.

903 Neal, J., Schumann, G., Bates, P.D.J.W.R.R., 2012. A simple model for simulating river
904 hydraulics and floodplain inundation over large and data sparse areas. 48.

905 Niedda, M.J.W.R.R., 2004. Upscaling hydraulic conductivity by means of entropy of terrain
906 curvature representation. 40(4).

907 Oleson, K. et al., 2008. Improvements to the Community Land Model and their impact on the
908 hydrological cycle. 113(G1).

909 Oleson, K. et al., 2013. Technical Description of version 4.5 of the Community Land Model
910 (CLM) (NCAR Technical Note No. NCAR/TN-503+ STR). Citeseer. National Center for
911 Atmospheric Research, PO Box, 3000: 555.

912 Owe, M., de Jeu, R., Holmes, T.J.J.o.G.R.E.S., 2008. Multisensor historical climatology of
913 satellite-derived global land surface moisture. 113(F1).

914 O'Neill, M.M., Tijerina, D.T., Condon, L.E., Maxwell, R.M., 2021. Assessment of the ParFlow–
915 CLM CONUS 1.0 integrated hydrologic model: evaluation of hyper-resolution water balance
916 components across the contiguous United States. Geoscientific Model Development, 14(12):
917 7223-7254.

918 Panday, S., Huyakorn, P.S., 2004. A fully coupled physically-based spatially-distributed model
919 for evaluating surface/subsurface flow. Advances in water Resources, 27(4): 361-382.

920 Ren, D., Xue, M.J.J.o.A.M., 2004. A revised force–restore model for land surface modeling.
921 43(11): 1768-1782.

922 Richards, L.A., 1931. Capillary conduction of liquids through porous mediums. Physics, 1(5):
923 318-333.

924 Rodell, M. et al., 2004. The global land data assimilation system. 85(3): 381-394.

925 Schaap, M.G., Leij, F.J.J.S.S., 1998. Database-related accuracy and uncertainty of pedotransfer
926 functions. 163(10): 765-779.

927 Seck, A., Welty, C., Maxwell, R.M., 2015. Spin-up behavior and effects of initial conditions for
928 an integrated hydrologic model. Water Resources Research, 51(4): 2188-2210.

929 Schalge, B., Haefliger, V., Kollet, S., Simmer, C.J.H.p., 2019. Improvement of surface run-off in
930 the hydrological model ParFlow by a scale-consistent river parameterization. 33(14): 2006-2019.

931 Schellekens, J., 2014. OpenStreams wflow documentation release 1.0 RC1. Deltares.

932 Shi, Y., Davis, K.J., Zhang, F., Duffy, C.J.J.J.o.H., 2014. Evaluation of the parameter
933 sensitivities of a coupled land surface hydrologic model at a critical zone observatory. 15(1):
934 279-299.

935 Shinozuka, M.J.J.o.S.E., 1983. Basic analysis of structural safety. 109(3): 721-740.

936 Shrestha, P., Sulis, M., Simmer, C., Kollet, S.J.H., Sciences, E.S., 2015. Impacts of grid
937 resolution on surface energy fluxes simulated with an integrated surface-groundwater flow
938 model. 19(10): 4317-4326.

939 Simmer, C. et al., 2016. Herz: The german hans-ertel centre for weather research. 97(6): 1057-
940 1068.

941 Simmons, C.T., Brunner, P., Therrien, R., Sudicky, E.A.J.J.o.H., 2020. Commemorating the 50th
942 anniversary of the Freeze and Harlan (1969) Blueprint for a physically-based, digitaFilly-
943 simulated hydrologic response model. 584: 124309.

944 Soltani, S.S., Ataie-Ashtiani, B., Danesh-Yazdi, M., Simmons, C.T.J.J.o.H., 2020. A
945 probabilistic framework for water budget estimation in low runoff regions: A case study of the
946 central Basin of Iran. 586: 124898.

947 Soltani, S.S., Ataie-Ashtiani, B., Simmons, C.T.J.E.-S.R., 2021. Review of assimilating GRACE
948 terrestrial water storage data into hydrological models: Advances, challenges and opportunities.
949 213: 103487.

950 Springer, A., Eicker, A., Bettge, A., Kusche, J., Hense, A.J.W., 2017. Evaluation of the water
951 cycle in the European COSMO-REA6 reanalysis using GRACE. 9(4): 289.

952 Sutanudjaja, E.H. et al., 2011. Large-scale groundwater modeling using global datasets: a test
953 case for the Rhine-Meuse basin. 15(9): 2913-2935.

954 Sutanudjaja, E., Van Beek, L., De Jong, S., Van Geer, F., Bierkens, M.J.W.R.R., 2014.
955 Calibrating a large-extent high-resolution coupled groundwater-land surface model using soil
956 moisture and discharge data. 50(1): 687-705.

957 Sulis, M. et al., 2017. Coupling groundwater, vegetation, and atmospheric processes: A
958 comparison of two integrated models. Journal of Hydrometeorology, 18(5): 1489-1511.

959 Tangdamrongsub, N. et al., 2015. Data assimilation of GRACE terrestrial water storage
960 estimates into a regional hydrological model of the Rhine River basin. 19(4): 2079-2100.

961 Therrien, R., McLaren, R., Sudicky, E., Panday, S., 2010. A three-dimensional numerical model
962 describing fully-integrated subsurface and surface flow and solute transport. User Guide.

963 Thierion, C. et al., 2012. Assessing the water balance of the Upper Rhine Graben hydrosystem.
964 424: 68-83.

965 Tóth, B. et al., 2015. New generation of hydraulic pedotransfer functions for Europe. 66(1): 226-
966 238.

967 Van Beek, L., Bierkens, M., 2009. The global hydrological model PCR-GLOBWB:
968 conceptualization, parameterization and verification. Utrecht University, Utrecht, The
969 Netherlands, 1: 25-26.

970 Van Dijk, A.I., Peña-Arancibia, J.L., Wood, E.F., Sheffield, J., Beck, H.E.J.W.R.R., 2013.
971 Global analysis of seasonal streamflow predictability using an ensemble prediction system and
972 observations from 6192 small catchments worldwide. 49(5): 2729-2746.

973 Van Genuchten, M.T., 1980. A closed-form equation for predicting the hydraulic conductivity of
974 unsaturated soils. Soil science society of America journal, 44(5): 892-898.

975 Wagner, W. et al., 2013. The ASCAT soil moisture product: A review of its specifications,
976 validation results, and emerging applications.

977 Wahl, S. et al., 2017. A novel convective-scale regional reanalysis COSMO-REA2: Improving
978 the representation of precipitation. 26(4): 345-361.

979 Wood, E.F. et al., 2011. Hyperresolution global land surface modeling: Meeting a grand
980 challenge for monitoring Earth's terrestrial water. 47(5).

981 Williams III, J.L., Maxwell, R.M., Monache, L.D.J.J.o.A.i.M.E.S., 2013. Development and
982 verification of a new wind speed forecasting system using an ensemble Kalman filter data
983 assimilation technique in a fully coupled hydrologic and atmospheric model. 5(4): 785-800.

984 Zhang, Y., Der Kiureghian, A., 1997. Finite element reliability methods for inelastic structures.
985 Department of Civil and Environmental Engineering, University of California.

a

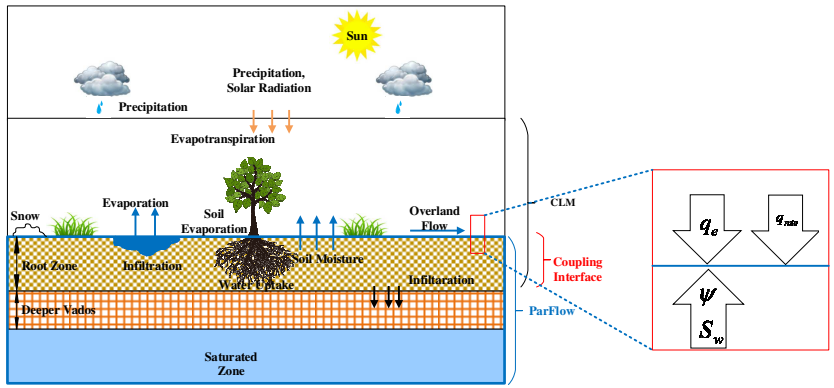
Sun
Precipitation, Solar Radiation
Precipitation
Evapotranspiration
Evaporation
Soil Evaporation
Snow
Overland Flow
Root Zone
Infiltration
Soil Moisture
Water Uptake
Infiltration
Deeper Vados
Saturated Zone
CLM
Coupling Interface
ParFlow
q_e
q_{rain}
ψ
S_w

b

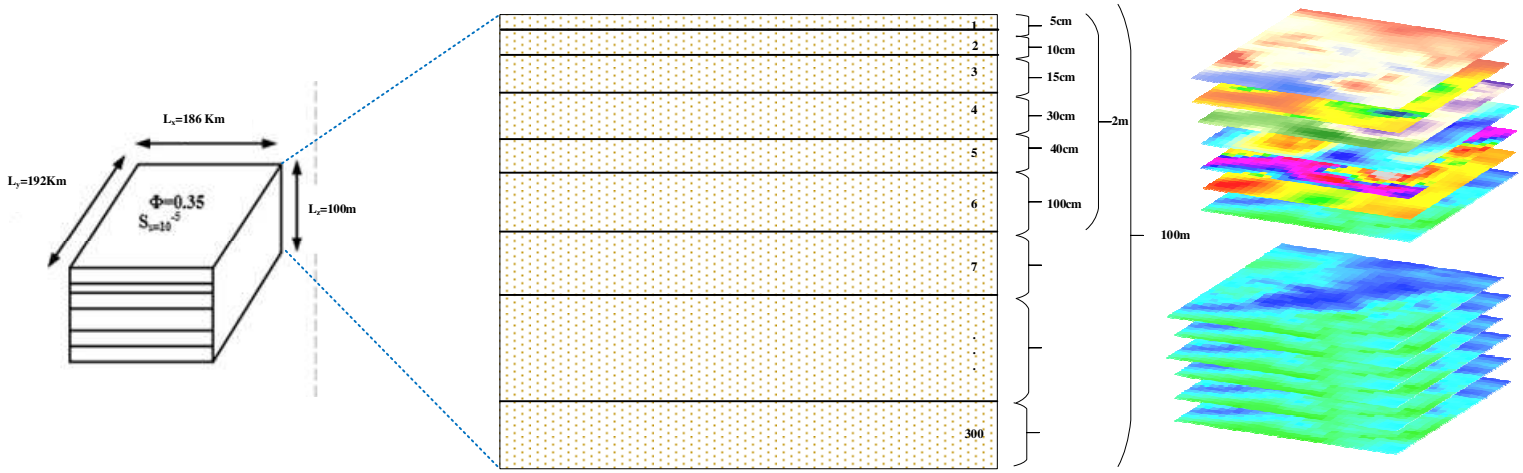
L_x=186 Km
L_y=192Km
L_z=100m
Φ=0.35
$S_{s=10^{-5}}$
1
2
3
4
5
6
7
300
5cm
10cm
15cm
30cm
40cm
100cm
2m
100m